Surfing Algorithm: Agile and Safe Transition Strategy for Hybrid Aerial Underwater Vehicle in Waves

Yuanbo Bi, Yufei Jin, *Graduate Student Member, IEEE*, Hexiong Zhou, Yulin Bai, Chenxin Lyu, *Graduate Student Member, IEEE*, Zheng Zeng, *Senior Member, IEEE*, and Lian Lian, *Senior Member, IEEE*

***Abstract*—The agile and safe transdomain in waves is a promising feature but the primary bottleneck of the hybrid aerial underwater vehicle (HAUV). In this article, the surfing algorithm is proposed for Nezha-mini, our predeveloped HAUV prototype, to search for the dynamic window facilitating takeoff in waves and avoiding hazardous waves. For the first time, the cross-domain window, i.e., the vehicle is at the wave crest and heading downstream, is characterized and defined through the vehicle-wave coupled dynamic model. The novel surfing algorithm consists of the gradient perceptron, time-limited momentum gradient search, heading server, and initial conditions. Nezha-mini senses, searches, and tracks the dynamic window in real-time, until the takeoff decisions are triggered. Numerical simulations and experiments in regular and irregular waves reveal the effectiveness of the algorithm. The vehicle maintains a healthy initial attitude and inaccessible wave disturbance during takeoff, thus alleviating the thrust distraction from stability recovery and uncertainty. The average transition time and energy cost are reduced by 59.2% and 26.1% compared with random takeoff cases, and the locomotion is smooth, graceful, and low-risk. The computation and cost are low as the algorithm only requires the basic flight controller and the data from the inertial measurement unit instead of the prior parameters of the HAUV and waves. In comparison with the adaptive robust controller, which resists wave disturbance directly, this article provides an enlightening strategy from the perspective of harnessing waves.**

***Index Terms*—Crossing wave surface, dynamic window, hybrid aerial underwater vehicle (HAUV), surfing algorithm (SA).**

Manuscript received 27 May 2023; revised 15 August 2023 and 19 September 2023; accepted 24 September 2023. This paper was recommended for publication by Associate Editor M. Fallon and Editor M. Yim upon evaluation of the reviewers' comments. This work was supported in part by the Science and Technology Commission of Shanghai Municipality Project under Grant 20dz1206600, in part by the Natural Science Foundation of Shanghai under Grant 20ZR1424800, in part by the Oceanic Interdisciplinary Program of Shanghai Jiao Tong University under Grant SL2022ZD106, and also in part by the China Postdoctoral Science Foundation under Grant 2023TQ0214. *(Corresponding author: Zheng Zeng.)*

Yuanbo Bi, Yufei Jin, Hexiong Zhou, Yulin Bai, and Chenxin Lyu are with the School of Oceanography, Shanghai Jiao Tong University, Shanghai 200240, China (e-mail: biyuanbo@sjtu.edu.cn; jinyufei00@sjtu.edu.cn; zhou_hexiong@sjtu.edu.cn; bylsjtu@sjtu.edu.cn; lvchenxin@sjtu.edu.cn).

Zheng Zeng and Lian Lian are with the School of Oceanography, Shanghai Jiao Tong University, Shanghai 200240, China, and also with the State Key Laboratory of Ocean Sciences, Shanghai Jiao Tong University, Shanghai 200240, China (e-mail: zheng.zeng@sjtu.edu.cn; llian@sjtu.edu.cn).

This article has supplementary material provided by the authors and color versions of one or more figures available at https://doi.org/10.1109/TRO.2023.3319928.

Digital Object Identifier 10.1109/TRO.2023.3319928

I. Introduction

THE hybrid aerial underwater vehicle (HAUV) has been a rapidly growing field of robotics research in the past decade [1]. The HAUVs have promising features such as flight-dive integration, convenient deployment, and recovery. Considerable application potential for HAUV has emerged in various 3-D missions at the air–water interface, including joint ocean observation, rapid emergency response, and covert military missions, due to the aforementioned benefits [2]. Cross-domain locomotion is the capability enabling the HAUV's transition from water to air and is crucial for amphibious tasks. How to ensure agile and safe cross-domain locomotion is an inevitable issue in the community of HAUVs.

However, waves bring more uncertainty than calm waters, making cross-domain operation much more difficult [3]. On the one hand, the aerodynamic and hydrodynamic parameters of HAUV do not intersect due to the diverse properties of water and air, such as the thrust and torque coefficients of the propeller, added mass, and center of buoyancy [4]. The dynamic wave surface further perturbs these parameters. On the other hand, the unpredictable disturbance and persistent swaying response [see, Fig. 1(a)] caused by waves restrict the initial conditions for takeoff. In addition, the dynamic characteristics of the actuator working in waves are complex [5], such as the generation of the water–air mixture [Fig. 1(b)] and cavitation [6]. This further amplifies the inherent instability of the system, inducing the vehicle to spin [see, Fig. 1(c)] or even capsize [see, Fig. 1(d)].

The HAUVs that exist across the world can be mainly categorized into three subsets, fixed-wing HAUVs, bio-inspired HAUVs, and multirotor HAUVs [7]. On account of the diversified implementation of these platforms, the unique cross-domain modalities of HAUVs with various configurations are driving the development of cross-domain strategy. For bio-inspired HAUVs, the typical cross-domain modes are wing-flapping [8], jet [9], and subduction [10]. The limited continuity and redundancy of the propulsion system impose restrictions on the anti-interference performance in wave environments. Besides, the wave slamming also poses a threat to the structural strength. Fixed-wing HAUVs have strong mobility and flexibility [11], [12]. But smooth cross-domain locomotion has relatively strict requirements on speed and attitude [13], and these constraints are harder to meet in waves than in calm water due to the

IEEE Transactions on Robotics (T-RO) paper, presented at ICRA 2024, Yokohama, Japan. Cite as T-RO paper.

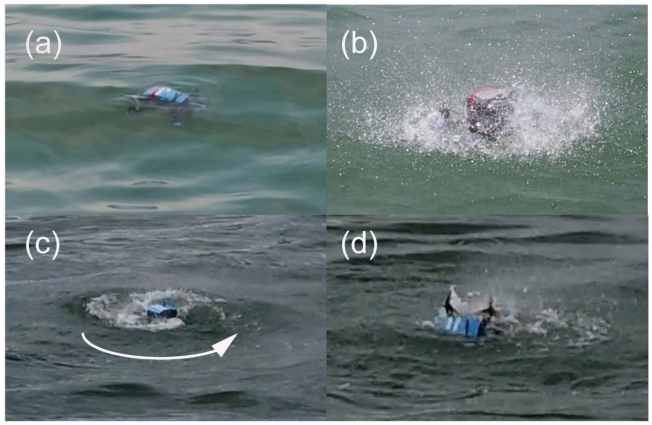

Fig. 1. Challenges and failures when HAUV crosses the wave surface. (a) Unhealthy initial attitude. (b) Actuators work in water–air mixed medium. (c) HAUV is spinning. (d) HAUV is capsizing.

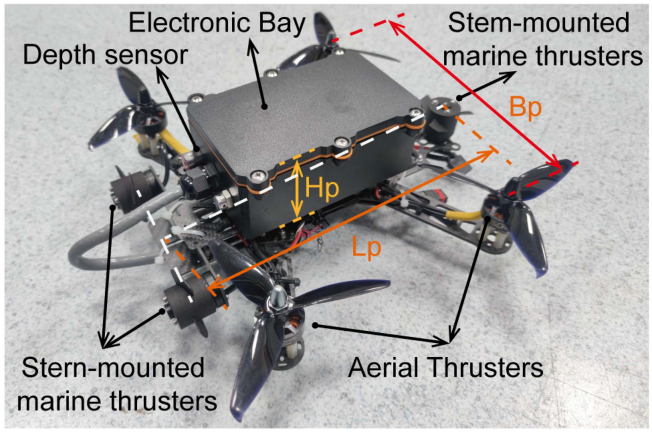

Fig. 2. Hardware setting except for the buoyancy material of the prototype HAUV: Nezha-mini.

continuous swaying. Gliding on the wave surface brings additional wave-induced resistance and further increases instability [14]. In contrast, the stable vertical takeoff and landing (VTOL) capability of multirotor HAUVs makes it a prospective pioneer in exploring the cross-domain strategies in waves [15], [16], [17].

Existing research on the cross-domain strategy of multirotor HAUVs mainly concentrates on the control scheme. Gain-scheduling proportional–integral–derivative (PID) control is easily available and widely used, which is favored by Naviator [18], Hydrone [19], Loon Copter [20], and other prototypes. The globally stable robust switching controller [21] and sliding mode controller [22] also demonstrate their applicability during the transition. Controllers with variable parameters that are not model-based have been verified to cope better with uncertainties, such as adaptive PID control [23] and fuzzy PID control [24]. The above research mostly remains in the stage of simulation and calm water test. For the VTOL mission of Nezha III in waves, a joint nonlinear controller composed of the adaptive dynamic surface controller [25], and nonlinear disturbance observer [26] is designed to enhance the robustness of the closed-loop system by estimating and compensating external disturbance caused by wind and waves. However, prototype tests have not been carried out yet. To sum up, at present, the successful experiment cases are mainly PID and related improvements in still water. Some control theories in waves are emerging, but rare tests have been implemented yet.

Beyond the control strategies that directly resist and adapt to wave disturbance, the cross-domain problem of HAUV in waves can be inspired by some novel dynamic window-searching approaches successfully implemented in the aviation and marine fields. Adaptive extended Kalman filter is applied to the collision perception and attitude recovery of unmanned aerial vehicle (UAV) [27]. Autoregressive time series prediction is used to estimate the quiescent periods of the carrier aircrafts taking off and landing on wave-affected deck [28], [29]. Long short-term memory network [30] is devoted to predicting the window of a submarine-launched folding UAV in oceanic conditions [31].

The contribution of this article lies in proposing a novel strategy for HAUV crossing the wave surface. The surfing algorithm (SA) is developed, simulated, and validated with the objective of facilitating agile and safe cross-domain movement. SA capitalizes on dynamic window-searching techniques and leverages real-time attitude data from the inertial measurement unit (IMU) to guide our prototype, Nezha-mini, through wave-induced dynamic windows. The unique propulsion layout of Nezha-mini enables the maneuvering heading server (HS) to search and track the window, and take off under the triggered conditions. Simulation and experiments reveal the effectiveness of the algorithm, which is significantly more time-saving and energy-saving compared with random takeoff. The cross-domain stability and safety are also improved. This article provides a strategy to harness the wave window, rather than try to resist wave disturbance directly.

The rest of this article is organized as follows. Section II delineates the wave-vehicle coupled dynamic model, drawing upon potential flow theory, wave inversion theory, rigid body dynamics, and finite element theory. In Section III, the mechanism and characteristics of the cross-domain dynamic window in waves are discussed. The framework and details of the SA are further proposed. Sections IV and V present simulation and performance evaluation experiments in both regular and irregular wave conditions, followed by comparative discussions. Finally, Section VI concludes this article.

II. Vehicle and Wave Dynamics

A. Prototype Overview

The prototype serving for the algorithm testing is named Nezha-mini. Design details and basic amphibious performance are discussed in our previous work [32]. For the iterative prototype exhibited in Fig. 2, the flight power and diving depth are further upgraded and the modular design facilitates the maintenance and algorithm debugging. The two stern-mounted marine thrusters fulfill the underwater maneuvering steering capability, which is the precondition of the implementation of the SA.

TABLE I
MAIN DESIGN PARAMETERS OF NEZHA-MINI

Symbol	Value	Unit
m	1.26	kg
$[L_p, B_p, H_p]$	[248, 206, 78]	mm
$[L, B, H]$	[140, 85, 60]	mm
$\omega_{\text{max,air}}$	1.78×10^4	rpm
$T_{\text{max,air}}$	520	g
V_{rate}	16.8	Volt

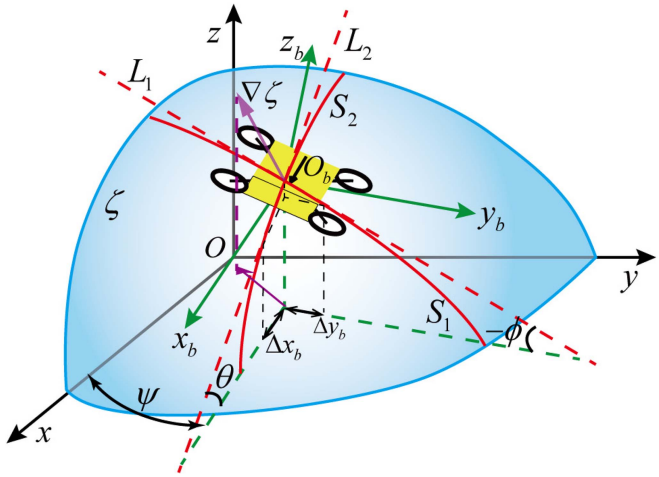

Fig. 3. Schematic diagram of coordinate systems and wave gradient vector. S_1 and S_2 are the intersection lines of $y_b o z_b$ plane and $x_b o z_b$ plane with wavy surface ζ, respectively. L_1 and L_2 are the tangents to S_1 and S_2 through the origin O_B of $\boldsymbol{R_B}$, respectively.

The main design parameters are tabulated in Table I, encompassing the mass m, the principal dimension $[L_p, B_p, H_p]$ (marked in the red, orange, and yellow lines in Fig. 2), the dimension of the electronic bay $[L, B, H]$, the maximum speed $\omega_{\text{max,air}}$, and thrust $T_{\text{max,air}}$ of a single aerial motor, and the power supply voltage V_{rate}. The carbon fiber structure of the vehicle is lightweight and produces minimal buoyancy, and the weight of the actuators is uniformly distributed with respect to the center of gravity (CG). Hence, the mathematical model of the HAUV is reduced to the size of the electronic bay.

B. Vehicle Dynamics

Two coordinate systems are needed when describing the locomotion characteristics of Nezha-mini, as shown in Fig. 3: The inertial frame $\{\boldsymbol{R_E}\}(O, x, y, z)$ and the body-fixed frame $\{\boldsymbol{R_B}\}(O_b, x_b, y_b, z_b)$. O is attached to the static water surface and O_b is fixed on CG of the vehicle. The position vector $\boldsymbol{\chi} = [x\ y\ z]^T$ and attitude vector $\boldsymbol{\Theta} = [\phi\ \theta\ \psi]^T$ are defined in $\{\boldsymbol{R_E}\}$, where ϕ, θ, and ψ are the roll, pitch, and yaw angles, respectively. The positive direction of the attitude and the coordinate axis satisfy the right-hand helix rule. $\boldsymbol{\upsilon} = [u\ v\ w]^T$ and $\boldsymbol{\Omega} = [p\ q\ r]^T$ are defined in $\{\boldsymbol{R_B}\}$, where u, v, and w are the velocities of the surge, sway, and heave, respectively, and p, q, and r are the angular velocities of roll, pitch, and yaw, respectively. The rotation matrix $\{\boldsymbol{R_1}\}$ and the transformation matrix of angular rate $\{\boldsymbol{R_2}\}$ expressing the transformation from $\{\boldsymbol{R_B}\}$ to $\{\boldsymbol{R_E}\}$ are given by

$$\boldsymbol{R_1} = \begin{bmatrix} c\theta c\psi & s\phi s\theta c\psi - c\phi s\psi & c\phi s\theta c\psi + s\phi s\psi \\ c\theta s\psi & s\phi s\theta s\psi + c\phi c\psi & c\phi s\theta s\psi - s\phi c\psi \\ -s\theta & s\phi c\theta & c\phi c\theta \end{bmatrix} \tag{1}$$

$$\boldsymbol{R_2} = \begin{bmatrix} 1 & s\phi t\theta & c\phi t\theta \\ 0 & c\phi & -s\phi \\ 0 & \frac{s\phi}{c\theta} & \frac{c\phi}{c\theta} \end{bmatrix} \tag{2}$$

where $c(\cdot)$, $s(\cdot)$, and $t(\cdot)$ denote $\cos(\cdot)$, $\sin(\cdot)$, and $\tan(\cdot)$ respectively. Notice that $\boldsymbol{R_1}^{-1} = \boldsymbol{R_1}^T$ since $\boldsymbol{R_1}$ is an orthogonal matrix. Therefore, the kinematic equation of the vehicle is

$$\dot{\boldsymbol{\chi}} = R_1 \boldsymbol{\upsilon},\ \dot{\boldsymbol{\Theta}} = R_2 \boldsymbol{\Omega}. \tag{3}$$

The multimodal dynamics for the vehicle under $\boldsymbol{R_B}$ are given based on the Newton–Euler equation

$$\begin{aligned}(\boldsymbol{M_0} - \varrho \boldsymbol{M_a})\dot{\boldsymbol{\upsilon}} - [(\boldsymbol{M_0} - \varrho \boldsymbol{M_a})\boldsymbol{\upsilon}] \times \boldsymbol{\Omega} - \varrho \boldsymbol{D_M} \boldsymbol{\upsilon}|\boldsymbol{\upsilon}| \\ + \boldsymbol{G_g} + \boldsymbol{F}_{\text{wave}} = (1 - \varrho)\boldsymbol{F}_{\text{air}} + \varrho \boldsymbol{F}_{\text{water}}\end{aligned} \tag{4}$$

$$\begin{aligned}(\boldsymbol{J_0} - \varrho \boldsymbol{J_a})\dot{\boldsymbol{\Omega}} + (\varrho \boldsymbol{M_a}\boldsymbol{\upsilon}) \times \boldsymbol{\upsilon} - [(\boldsymbol{J_0} - \varrho \boldsymbol{J_a})\boldsymbol{\Omega}] \times \boldsymbol{\Omega} \\ - \varrho \boldsymbol{D_J} \boldsymbol{\Omega}|\boldsymbol{\Omega}| + \boldsymbol{M}_{\text{wave}} = (1 - \varrho)\boldsymbol{M}_{\text{air}} + \varrho \boldsymbol{M}_{\text{water}}\end{aligned} \tag{5}$$

In (4) and (5), ϱ is the phase factor that $\varrho = 1$ means the submersed state and $\varrho = 0$ means the airborne state. m is the mass of HAUV and $\boldsymbol{M_0} = \text{diag}[m, m, m]$. $\boldsymbol{J_0} = \text{diag}[I_{xx}, I_{yy}, I_{zz}]$ is the moment of inertia around the x, y, and z axis of $\boldsymbol{R_B}$. Let the gravity vector in $\boldsymbol{R_B}$ of HAUV be $\boldsymbol{G_g} = J_1^T [0\ 0\ -mg]^T$, where $g = 9.8$ m/s^2 is the vertically downward acceleration of the gravity. The added mass and inertia of the 6 degrees of freedom (6DOF) in hydrodynamics are expressed as $\boldsymbol{M_a} = \text{diag}[X_{\dot{u}}, Y_{\dot{v}}, Z_{\dot{w}}]$ and $\boldsymbol{J_a} = \text{diag}[K_{\dot{p}}, M_{\dot{q}}, N_{\dot{r}}]$. The drag coefficients and drag moment coefficients are defined as $\boldsymbol{D_M} = \text{diag}[X_{u|u|}, Y_{v|v|}, Z_{w|w|}]$ and $\boldsymbol{D_J} = \text{diag}[K_{p|p|}, M_{q|q|}, N_{r|r|}]$ in 6DOF, respectively. During vehicle surfing, hydrodynamic parameters are time varying randomly. They are assumed to be time invariant for simulation, and the uncertainty is regarded as part of the wave disturbance. $\boldsymbol{F}_{\text{air}}$, $\boldsymbol{F}_{\text{water}}$ and $\boldsymbol{M}_{\text{air}}$, $\boldsymbol{M}_{\text{water}}$ are all 3×1 vectors that correspond to the control force and moment of the aerial and marine actuators, respectively. The wave force and moment to which the vehicle is subjected are $\boldsymbol{F}_{\text{wave}}$ and $\boldsymbol{M}_{\text{wave}}$, which is discussed in detail in Section II-C and II-D.

C. Wave Model

Consider the long-crested wave in deep water, then it is good to apply the airy wave theory. First, the wave model is established based on the following 4 hypotheses.

1) Potential Flow Hypothesis: The wave is the ideal fluid that is inviscous, irrotational, and incompressible.
2) Linear Microwave Hypothesis: The wave height is significantly smaller in relation to the wavelength.
3) Froude–Krylov Hypothesis: The presence of vehicles in a wave does not perturb the pressure distribution of the wave.
4) Minor Attitude Hypothesis: The attitude of the vehicle is minimal and the advanced velocity is low.

Based on the above hypotheses, the wave potential function $\Phi(x, y, z, t)$ can be solved analytically through the simultaneous governing equations of potential flow $\nabla^2\Phi = 0$ and the boundary conditions. $\Phi(x, y, z, t)$ has the following properties:

$$\begin{aligned} \zeta(x, y, z, t) &= -\frac{1}{g}\frac{\partial \Phi}{\partial t}\Big|_{z=0}, \; u_x(x, y, z, t) = \frac{\partial \Phi}{\partial x} \\ u_y(x, y, z, t) &= \frac{\partial \Phi}{\partial y}, \; u_z(x, y, z, t) = \frac{\partial \Phi}{\partial z} \end{aligned} \tag{6}$$

where u_x, u_y, u_z is the wave velocity at time t at the (x, y, z) coordinate along the x, y, z direction of the three coordinate axes in $\boldsymbol{R_E}$, and ζ is the height of the wave surface. Irregular waves can be regarded as the superposition of multiple regular waves with different frequencies and propagation directions. Hence, ζ can be described as follows according to the analytical solution of Φ and (6):

$$\begin{aligned} &\zeta(x, y, z, t) \\ &= \sum_{i=1}^{m}\sum_{j=1}^{n} h_{ij} e^{k_i z} \cos(k_i x \cos(\mu_j) + k_i y \sin(\mu_j) - \omega_i t + \varepsilon_{ij}) \end{aligned} \tag{7}$$

where, $\omega_i \in [\omega_{\min}, \omega_{\max}], i = 1, 2, \ldots m$ denotes the total m waves in the simulated frequency band, where $\omega_{\min}$ and $\omega_{\max}$ are the lower and upper bounds. Moreover, set the frequency band interval to $d\omega$. k_i indicates the wave number and we have $\omega_i^2 = k_i g$ according to the dispersion relations of deep water waves. $\mu_j \in [\mu_{\min}, \mu_{\max}], j = 1, 2, \ldots n$ denotes the whole n absolute wave directions of simulation in $\boldsymbol{R_E}$, where $\mu_{\min}$ and $\mu_{\max}$ are the lower and upper bounds, and the interval is $d\mu$. $\varepsilon_{ij} \sim U(0, 2\pi)$ is the $m \times n$ random initial wave phase that follows the uniform distribution in $[0, 2\pi]$. h_{ij} is the height of each regular wave and is also $m \times n$ matrix. Based on the wave spectrum theory, (8) indicates the connection between the wave amplitude and spectrum.

$$h_{ij} = \sqrt{2S(\omega_i, \mu_j)d\omega d\mu} = \sqrt{2S_\zeta(\omega_i)\varphi(\mu_j)d\omega d\mu} \tag{8}$$

where $S(\omega_i, \mu_j)$ reflects the wave energy distribution in different frequency bands and directions based on the statistical induction. It can be decomposed into the product of wave spectrum $S_\zeta(\omega)$ and direction spectrum $\varphi(\mu)$. They are essentially probability density functions that reflect the law of distribution. According to the recommendation of the International Towing Tank Conference, the two spectra can be expressed as

$$\begin{aligned} S_\zeta(\omega) &= \frac{173 h_{1/3}^2}{\overline{T}^4 \omega^5} \exp\left(-\frac{691}{\overline{T}^4 \omega^4}\right) \\ \varphi(\mu) &= \frac{2}{\pi}\cos^2(\mu) \end{aligned} \tag{9}$$

where $h_{1/3}$ and $\overline{T}$ are the significant height and average period of waves, respectively, which can be determined by the level of the wave state.

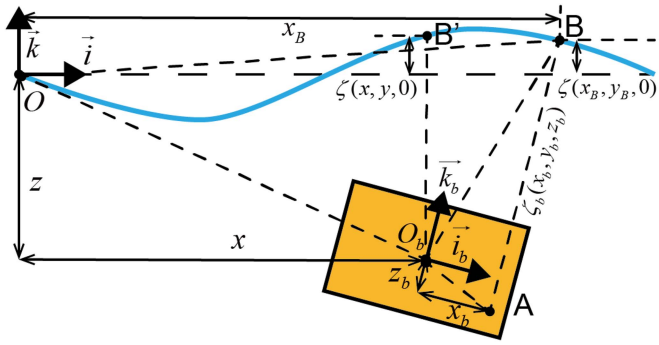

Fig. 4. Schematic diagram of coordinate transformation in wave surface with the height ζ. The vehicle is simplified as the orange cuboids. Dot A is an infinitesimal of the vehicle. The coordinate of A is (x_b, y_b, z_b) in $\boldsymbol{R_B}$. $\overline{AB}$ is the distance ζ_b between the wave surface and point A in $\boldsymbol{R_B}$ and $\overline{O_b B'}$ is the distance between the wave surface and point O_b in $\boldsymbol{R_E}$. The coordinates of dot B is $(x_B, y_B, \zeta(x_B, y_B, 0))$ in $\boldsymbol{R_E}$. $\vec{\boldsymbol{i}} = [1, 0, 0]^T, \vec{\boldsymbol{k}} = [0, 0, 1]^T$ and $\vec{\boldsymbol{i_b}}, \vec{\boldsymbol{k_b}}$ are the unit vectors of x, z axis and x_b, z_b axis respectively.

D. Wave Dynamics

The Navier–Stokes equation is reduced to the Bernoulli equation according to the potential flow hypothesis. Then, the pressure distribution $\Delta P(x, y, z, t)$ in $\boldsymbol{R_E}$ of the wave field (7) can be expressed as

$$\Delta P(x, y, z, t) = -\rho_w \frac{\partial \Phi}{\partial t} - \frac{1}{2}\rho_w \nabla\Phi \cdot \nabla\Phi - \rho_w g z \tag{10}$$

where ρ_w is the density of water. The first two terms on the right of the equals sign in (10) can be further derived from (6) and (7). The first term is related to the wave amplitude ζ and the second term is concerned with the wave velocity. Thus, ΔP represents the dynamic pressure caused by wave fluctuation. The last term in (10) refers to the static pressure, which generates the buoyancy of the vehicle.

According to the finite element theory, we discretize the vehicle into multiple microelements with intervals dx, dy, and dz in $\boldsymbol{R_B}$. However, ΔP and ζ are all in $\boldsymbol{R_E}$. Hence, they are required to be converted into $\boldsymbol{R_B}$, which is $\Delta P_b(x_b, y_b, z_b, t)$ and $\zeta_b(x_b, y_b, z_b, t)$.

As shown in the simplified geometric model in Fig. 4, we get $\overline{OO_b} + \overline{O_b B} = \overline{OB}$ in $\boldsymbol{R_E}$ from the geometric relation. Then the equation set (11) can be obtained as

$$\begin{bmatrix} x \\ y \\ z \end{bmatrix} + \boldsymbol{J_1} \begin{bmatrix} x_b \\ y_b \\ \zeta_b + z_b \end{bmatrix} = \begin{bmatrix} x_B \\ y_B \\ \zeta(x_B, y_B, 0) \end{bmatrix}. \tag{11}$$

As $\zeta(x_B, y_B, 0)$ is obtained from (7), there are three unsolved parameters of the three equations in (11), that are, x_B, y_B, and ζ_b. Only ζ_b is our concern. To reduce the computational burden and avoid the occurrence of no solution, based on hypotheses 2 and hypotheses 4, $\zeta(x_B, y_B, 0)$ can be approximated as $\zeta(x, y, 0)$, as shown in Fig. 4. Thus, the numerical solution of ζ_b can be acquired from the last row of (11), as shown in (12). Then ζ_b is substituted into (10) to get ΔP_b.

$$z + \{\boldsymbol{J_1}[x_b, y_b, \zeta_b + z_b]^T\}^T \vec{\boldsymbol{k}} = \zeta(x, y, 0). \tag{12}$$

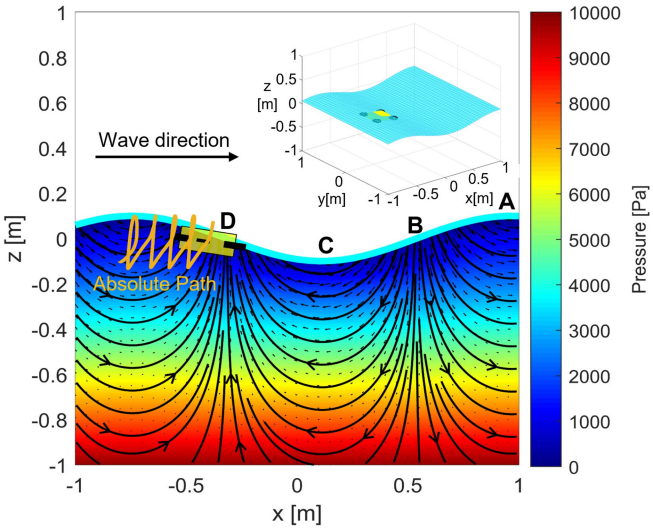

Fig. 5. Vertical pressure profile with the streamlines and the velocity vector of the wave particles for a single regular wave and the drifting response of the HAUV.

The wave force and moment acting on the vehicle are the integral of the pressure distribution $\Delta P_b(x_b, y_b, z_b, t)$ along the wet surface S_{wet} of the vehicle. By virtue of Gauss's formula, the integral along S_{wet} can be transformed to the integral along the immersed volume V_{wet}.

$$\begin{aligned} \boldsymbol{F}_{\text{wave}} &= -\iint_{S_{\text{wet}}} (\Delta P_b)\vec{\boldsymbol{n}} dS = -\iiint_{V_{\text{wet}}} \nabla(\Delta P_b) dV \\ \boldsymbol{M}_{\text{wave}} &= -\iint_{S_{\text{wet}}} (\Delta P_b)\vec{\boldsymbol{r}} \times \vec{\boldsymbol{n}} dS \\ &= -\iiint_{V_{\text{wet}}} \nabla \times (\Delta P_b \vec{\boldsymbol{r}}) dV \end{aligned} \tag{13}$$

where, $\vec{\boldsymbol{n}}$ is the unit normal vector to S_{wet}, pointing out of S_{wet}. $\vec{\boldsymbol{r}}$ is the position vector of the vehicle's infinitesimal in $\boldsymbol{R_B}$. The wave-vehicle coupled model is based on (3)–(5) and (13).

III. Algorithm and Methodology

A. Takeoff Window

The stationary degree of wave surface affects the stability and safety of the cross-domain locomotion when the aerial propellers are subject to random and inevitable immersion, as summarized in our early research [33]. Based on the superposition principle, the conclusion of the single regular waves is also applicable to irregular waves. The single wave with $\omega = 6$ rad/s and $h = 0.06$ m in Section II, without considering the noise disturbance, is used to explore the mechanism of the potential takeoff window. Fig. 5 shows the vertical pressure profile with the streamlines and the velocity vector of the wave particles. The absolute path in $\boldsymbol{R_E}$ that the vehicle drifts, marked as the yellow line, is a forward spiral that resembles the moving path of the wave particle. The pressure gradient of the subsurface shapes, similar to the undulation of the wave surface, decays with depth and is nearly flat at depths less than 0.6 m. Four typical positions A to D are marked, denoting the crest, descending point, trough, and ascending point, respectively.

Take the roll channel in (5) as an example and ignore the coupling term. Consider, the tilt angle ϕ for an instantaneous state of the vehicle in a transverse wave $\zeta = \zeta_0 \cos(ky - \omega t)$. The tilt angle of the wave surface is κ. According to hypothesis 2, $\kappa = \frac{\partial \zeta}{\partial y}|_{y=y_b} = \kappa_0 \sin \omega t$, and $\sin(\phi - \kappa) \approx (\phi - \kappa)$, where $\kappa_0 = k\zeta_0$. The equation of rolling motion is simplified as follows:

$$\ddot{\phi} + \upsilon_\phi \dot{\phi} + n_\phi^2 \phi = \kappa_0 n_\phi^2 \sin \omega t \tag{14}$$

where, $\upsilon_\phi = \frac{K_{p|p|}}{I_{xx} + K_{\dot{p}}}$ is the coefficient of roll damping and $n_\phi = \sqrt{\frac{Dh}{I_{xx} + K_{\dot{p}}}}$ is the inherent frequency of roll. These two parameters are only related to the vehicle design. D is the vehicle displacement and h is the initial metacentric height. The particular solution of the roll equation is denoted by $\phi = K_{\phi\kappa}\kappa_0 \sin(\omega t + \varepsilon_{\phi\kappa})$, where $K_{\phi\kappa}$ is the amplitude–frequency response function and $\varepsilon_{\phi\kappa}$ is the phase-frequency response function.

$$\begin{aligned} K_{\phi\kappa}(\Lambda) &= \frac{1}{\sqrt{(1-\Lambda^2)^2 + \mu_\phi^2 \Lambda^2}} \\ \varepsilon_{\phi\kappa}(\Lambda) &= \arctan\left(-\frac{\mu_\phi \Lambda}{1-\Lambda^2}\right) \end{aligned} \tag{15}$$

where, $\mu_\phi = \upsilon_\phi / n_\phi$, and $\Lambda = \omega / n_\phi$ is the relative frequency of the wave to the vehicle. For miniature vehicles, such as Nezha-mini, n_ϕ is relatively large compared with general wave frequency, thus, $\Lambda \ll 1$, $\mu_\phi \in (0, 1)$. Both, $K_{\phi\kappa}$ and $\varepsilon_{\phi\kappa}$ are monotonically increasing functions in the above range and $\varepsilon_{\phi\kappa} \to 0$. When the vehicle heading is at an angle χ to the wave direction with an advanced speed u, the roll-response frequency is no longer the wave frequency, but the encounter frequency $\omega_e = \omega + \frac{\omega^2}{g} u \cos \chi$, thus, $\Lambda = \omega_e / n_\phi$.

When the vehicle surfs, $\chi = \pi$ and $\omega_e < \omega$, thus, both $K_{\phi\kappa}$ and $\varepsilon_{\phi\kappa}$ decrease. Hence, the vehicle's roll is reduced. Conversely, the roll will increase as the vehicle travels in opposition to the wave direction, which hinders the takeoff.

When the vehicle is at the crest (point A in Fig. 5), $\omega t = 2n\pi$ and $\phi_0 = K_{\phi\kappa}\kappa_0 \sin \varepsilon_{\phi\kappa}$. When the vehicle is at points BD, $\omega t = \pm\pi/2 + 2n\pi$ and $\phi_1 = K_{\phi\kappa}\kappa_0 \cos \varepsilon_{\phi\kappa} > \phi_0$ at this time. When the vehicle is at the trough (point C), $\omega t = \pi + 2n\pi$ and $\phi_2 = -\phi_0$. Hence, the roll at A and C points is lower than that of B and D points. From the point of view of wave particle velocity analysis, the particle velocity at x_b direction is $u_x = \omega\zeta_0 \cos(kx - \omega t)$, according to (6). The direction of the particle velocity at the wave crest is parallel to the surfing direction, which provides an initial speed that avails of the waves after takeoff, whereas the velocity direction is opposite at the trough. Thus takeoff at the crest has a speed advantage over the trough. Besides, the vertical velocity u_z is stationary. The rising inertia of the vehicle and the subsequent dropping wave create favorable conditions for takeoff at the crest.

Regrettably, the precise heave response cannot be obtained after two acceleration integrations due to the unavoidable measurement noise of the low-cost IMU. It is also challenging to

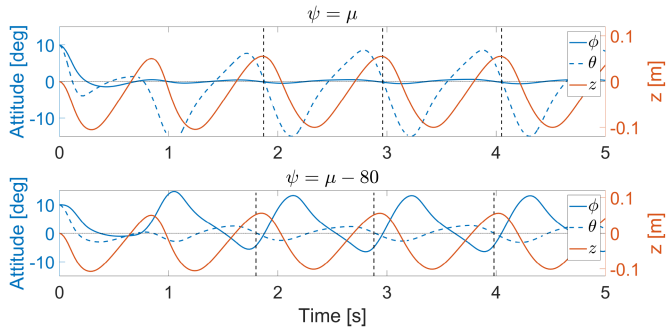

Fig. 6. Relation of vehicle heading and heave response.

accurately capture the wave position in irregular waves using merely the acceleration trend. $\phi = \mu$ and $\phi = \mu - 80°$ are simulated under the same regular wave to explore the relation of the attitude and heave response for determining the dynamic window. The results are shown in Fig. 6. The roll channel is leveled off due to the minor wave moment when the vehicle is following the wave. Therefore, only the pitch channel requires attention, which is equivalent to decreasing the complexity of the takeoff process by 1D. On the basis of roll convergence, when the pitch changes from positive to negative (i.e., the downward zero-crossing), the heave is the highest and the vehicle is at the crest. However, the roll and pitch both change when $\psi \neq \mu$. As the trend of attitude variation is inapparent, it is difficult to determine whether or not the vehicle is at the wave crest. For example, the robot is situated ahead of the wave crest at the downward zero crossing of pitch, as shown in the dotted black line of the second subplot of Fig. 6. Based on the analysis of simulation results, we obtain the following sufficient conditions:

When the vehicle's heading coincides with the wave direction, the vehicle is signified at the crest if the roll of the vehicle tends to be stable and, meanwhile, the pitch is at the downward zero crossing.

The inference above can be expressed in (16).

$$\left.\begin{array}{l} |\phi[t]| \leq \phi_{\text{lim}} \quad \forall t \in \Xi \\ (\theta[k-1] > 0)\&\&(\theta[k] < 0) \\ \psi[\Xi] \subseteq \{\psi \mid |\psi - \psi_d[k]| \leq \psi_{\text{lim}}\}, \end{array}\right\} \Rightarrow z[k] \rightarrow z_{\text{lmax}} \quad (16)$$

where k is the number of current iteration steps and n is the maximum length of the takeoff window. $\Xi = \{t \mid t[k-n] \leq t \leq t[k]\}$ is the left neighborhood of the current time $t[k]$ with the length of n. ϕ_{lim} is the upper limit of the roll range allowed for takeoff. ψ_{lim} is the ceiling for determining the stability of the heading error. ϕ_{lim} and ψ_{lim} are both set at 3°. z_{lmax} means the local maximum point of the heave response. ψ_d is the estimated wave direction. The takeoff window is allowed if (16) is satisfied in Ξ. Hereby, (16) is considered as the *takeoff constraints*. Consequently, the SA is required to keep ψ_d and the actual wave direction μ as close as possible to ensure the presence of a takeoff window.

B. Algorithm Framework

1) Gradient Perceptron: When the vehicle is drifting on the wave surface without control, similar to hypothesis 4, we assume that

a) *Slippage hypothesis:* The bottom of the vehicle remains tangent to the plane of the wave surface.

Let the position of the vehicle in $\boldsymbol{R_E}$ and $\boldsymbol{R_B}$ at time t_k be $\boldsymbol{X_k} = [x_k, y_k]$ and $\boldsymbol{X_b} = [x_{bk}, y_{bk}]$, respectively. The wave surface ζ in $\boldsymbol{R_E}$ is assumed to be continuous, and its second partial derivative exists and is continuous. The wave surface in $\boldsymbol{R_B}$ is ζ_b and meets $\zeta(\boldsymbol{X_k}) = \zeta_b(\boldsymbol{X_b})$. The second-order Taylor expansion of ζ_b at $\boldsymbol{X_b}$ yields the following:

$$\begin{aligned} \zeta_b(x_b, y_b) = \zeta_b(\boldsymbol{X_b}) + \left[\frac{\partial \zeta_b}{\partial x_b}, \frac{\partial \zeta_b}{\partial y_b}\right]_{\boldsymbol{X_b}} \Delta \boldsymbol{X_b} \\ + \frac{1}{2!} \Delta \boldsymbol{X_b}^T H(\boldsymbol{X_b}) \Delta \boldsymbol{X_b} + O(\Delta \boldsymbol{X_b}^2) \\ H(\boldsymbol{X_b}) = \left[\begin{array}{cc} \frac{\partial^2 \zeta_b}{\partial x_b^2} & \frac{\partial^2 \zeta_b}{\partial x_b y_b} \\ \frac{\partial^2 \zeta_b}{\partial y_b x_b} & \frac{\partial^2 \zeta_b}{\partial y_b^2} \end{array}\right]_{\boldsymbol{X_b}} \end{aligned} \quad (17)$$

where $\Delta \boldsymbol{X_b} = [x_b - x_{bk} \ y_b - y_{bk}]^T$, $O(\Delta \boldsymbol{X_b}^2)$ is the higher order infinitesimals of $\Delta \boldsymbol{X_b}$. Ignoring the second-order and higher order terms in (17), the gradient vector of the wave surface $\boldsymbol{\nabla \zeta_b}$ in $\boldsymbol{R_B}$ can be expressed as $\boldsymbol{\nabla \zeta_b}(\boldsymbol{X_b}) = \left[\frac{\partial \zeta_b}{\partial x_b}, \frac{\partial \zeta_b}{\partial y_b}\right]^T_{\boldsymbol{X_b}}$.

As shown in Fig. 3, the vehicle attitude at t_k is $[\phi, \theta, \psi]^T$. The acute angle between L_2 and x_b axis is θ, and the acute angle between L_1 and y_b axis is $-\phi$. Δt is the interval from time t_{k-1} to t_k. The vehicle displacement in $\boldsymbol{R_B}$ during Δt is $\Delta x_b, \Delta y_b \rightarrow 0$. According to the definition of partial derivatives, and combining hypothesis 5 and geometric relations, we have

$$\begin{aligned} \left.\frac{\partial \zeta_b}{\partial x_b}\right|_{\boldsymbol{X_b}} &= \lim_{\Delta x_b \rightarrow 0} \frac{\zeta_b(x_{bk} + \Delta x_b, y_{bk}) - \zeta_b(x_{bk}, y_{bk})}{\Delta x_b} \\ &= \tan(\pi - \theta) \\ \left.\frac{\partial \zeta_b}{\partial y_b}\right|_{\boldsymbol{X_b}} &= \lim_{\Delta y_b \rightarrow 0} \frac{\zeta_b(x_{bk}, y_{bk} + \Delta y_b) - \zeta_b(x_{bk}, y_{bk})}{\Delta y_b} \\ &= \tan(\pi + \phi). \end{aligned} \quad (18)$$

The transition matrix with respect to ψ form $\boldsymbol{R_B}$ to $\boldsymbol{R_E}$ is given by $\boldsymbol{J(\psi)} = \begin{bmatrix} \cos(\psi) & -\sin(\psi) \\ \sin(\psi) & \cos(\psi) \end{bmatrix}$. Hence, we have $\boldsymbol{\nabla \zeta}(\boldsymbol{X_k}) = \boldsymbol{J(\psi)} \boldsymbol{\nabla \zeta_b}(\boldsymbol{X_b})$. Denote α as the argument of $\boldsymbol{\nabla \zeta}$ in the xoy plane, we have $\alpha = \text{atan2}[\ (\boldsymbol{\nabla \zeta})^T \vec{\boldsymbol{j}},\ (\boldsymbol{\nabla \zeta})^T \vec{\boldsymbol{i}}\ ]$.

The vehicle attitude changes continually as the wave surface heaves, resulting in a persistent shift in α. When $||\boldsymbol{\nabla \zeta}||$ achieves a local maximum, the corresponding α is selected as the most probable tracking direction because the effect of the wave on the vehicle attitude can be considered maximum at this time. The scenario may be a higher or closer wave around the vehicle, which indicates that the wave is the most valuable and representative to track. The high-frequency disordered waves bring noise or uncharacterized local maxima to $||\boldsymbol{\nabla \zeta}||$ inevitably, and then interfere with the judgment of the local maximum.

Algorithm 1: Gradient Perceptron (GP).

Input: Current attitude ϕ, θ, ψ
Output: α, $\|\widetilde{\nabla\zeta}\|$
1: Get $\nabla\zeta_b$ from (18)
2: $\nabla\zeta = \boldsymbol{J}(\psi)\nabla\zeta_b$
3: $\alpha = \text{atan2}[(\nabla\zeta)^T\vec{j},\ (\nabla\zeta)^T\vec{i}]$
4: $\|\widetilde{\nabla\zeta}\| =$ **Kalman Filter**$(\|\nabla\zeta\|)$

Algorithm 2: Kalman Filter (KF).

Input: Raw data Ψ
Output: Filtered data $\widetilde{\Psi}$
1: static initial Ψ_{last}, P
2: const variance of process noise $Q = 0.25$ and variance of measurement noise $R = 0.75$
3: Get variance of prediction $P_{\text{est}} = P + Q$
4: Get Kalman gain $K_g = \frac{P_{\text{est}}}{P_{\text{est}}+R}$
5: Get predictive value $\widetilde{\Psi} = \Psi_{\text{last}} + K_g(\Psi - \Psi_{\text{last}})$
6: Update variance of estimation $P = (1 - K_g)P_{\text{est}}$
7: Record $\Psi_{\text{last}} = \widetilde{\Psi}$

Kalman filter is applied to $||\nabla\zeta||$ to get smooth $||\widetilde{\nabla\zeta}||$ and improve the accuracy of wave tracking, as shown in Algorithm 1 and 2. The SA only uses a 1-D Kalman filter for the wave gradient data, which is simple in principle, small in memory, and fast in calculation. The *steering constraints* based on the local maximum criteria are expressed as follows:

$$\left.\begin{array}{l}(\|\widetilde{\nabla\zeta}\|'[k] < 0)\ \&\&\ \left(\|\widetilde{\nabla\zeta}\|'[k-1] > 0\right)\\ \|\widetilde{\nabla\zeta}\|[k] \geq \|\nabla\zeta\|_{\text{lim}}\\ |\psi_d[k] - \psi[k]| \leq \psi_{\text{lim}}\end{array}\right\}$$
$$\Rightarrow \|\nabla\zeta\|[k-1] \rightarrow \|\nabla\zeta\|_{\text{lmax}} \tag{19}$$

In (19), except for the local maximum criteria (the first constraint), two additional constraints are added based on the feedback during our field test. The second constraint serves to further attenuate the noise based on the Kalman filter. If the average swing amplitude of the vehicle caused by the wave is less than $\vartheta°$, it is considered noise and the steering is not permitted. Thus, $\|\nabla\zeta\|_{\text{lim}}$ means the lower bound of wave-induced effects on the vehicle, and $\|\nabla\zeta\|_{\text{lim}} \triangleq \sqrt{\tan(\vartheta)^2 + \tan(\vartheta)^2}$. ϑ can be adjusted depending on the wave state. The third constraint is to ensure that the vehicle's heading has converged, that is, the steering toward the last desired heading has been attained. The stern-mounted marine thrusters do not coincide strictly with the horizontal plane where the vehicle's CG is located, resulting in undesired attitude changes during steering. Nevertheless, the algorithm expects that all variations in attitude are solely attributable to the presence of waves. Therefore, the third constraint can filter the noise generated during the steering.

2) Time-Limited Momentum Gradient Search: It is greedy to directly adopt the estimated wave direction α corresponding to $\|\nabla\zeta\|_{\text{lmax}}$ as the updated heading. Thus, a part of the conservative inertia is added and the time-limited momentum gradient search (TMGS) algorithm is introduced in Algorithm 3.

Algorithm 3: Time-Limited Momentum Gradient Search (TMGS).

Input: Estimated wave direction α, current heading ψ
Output: Updated tracking heading ψ_d
1: static initial last desired heading $\psi_{d\text{last}}$, iteration number $k = 0$
2: $e_{\alpha\psi} = \alpha - \psi$
3: **if Acute angle constraint (20)** are satisfied **then**
4: $\quad\overline{e_{\alpha\psi}} = |e_{\alpha\psi} - \text{sgn}[e_{\alpha\psi}(|e_{\alpha\psi}| > 3\pi/2)] \times 2\pi|/(\pi/2)$
5: $\quad\gamma = 1 - e^{-0.3\ k}$
6: $\quad\beta = (1 - \tanh[3(1 - \overline{e_{\alpha\psi}})])\gamma$
7: $\quad\psi_d = \arg[\beta e^{i\psi_{d\text{last}}} + (1-\beta)e^{i\alpha}]$
8: $\quad\psi_{d\text{last}} = \psi_d,\ k++$
9: **end if**

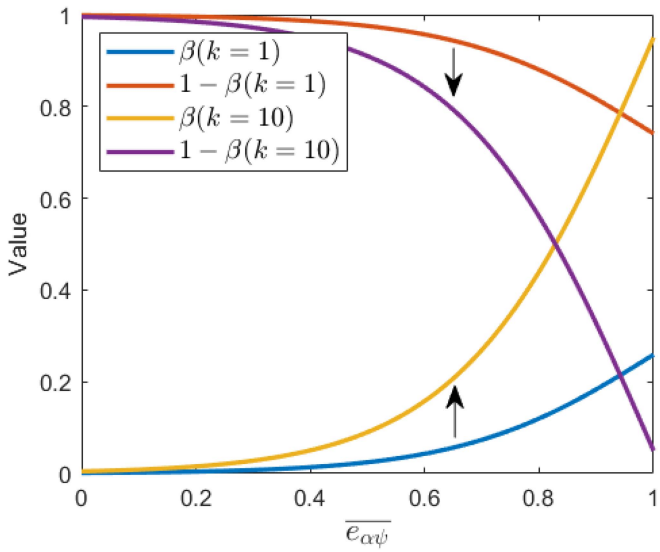

Fig. 7. Graph of inertia factor β versus time and absolute error $\overline{e_{\alpha\psi}}$.

To avoid the vehicle spiraling in waves, the *acute angle constraint*, expressed mathematically in (20) is proposed. It indicates that the desired heading ψ_d is not updated, until the error $e_{\alpha\psi}$ between the estimated wave direction α and current heading $\psi(\psi \in ([-\pi, \pi]))$ is an acute angle. Then, the normalized error $\overline{e_{\alpha\psi}}$ is gained in line 4 of Algorithm 3. The range [0,1] of $\overline{e_{\alpha\psi}}$ means the absolute error from 0 to $\pi/2$.

$$\text{s.t.}(|e_{\alpha\psi}| < \pi/2)\ ||\ (|e_{\alpha\psi}| > 3\pi/2). \tag{20}$$

The desired heading ψ_d is updated through line 7. ψ_d is the argument of the linear combination of two direction vectors about $\psi_{d\text{last}}$ and α, with i representing the imaginary part. Inspired by the activation function in neural networks, the inertia factor β can be expressed as line 6. A larger β means a larger weight on $\psi_{d\text{last}}$, that is, a more conservative estimation of heading. Furthermore, the time-limited factor γ is introduced to β, and the image is shown in Fig. 7. In the initial period, the estimation of heading

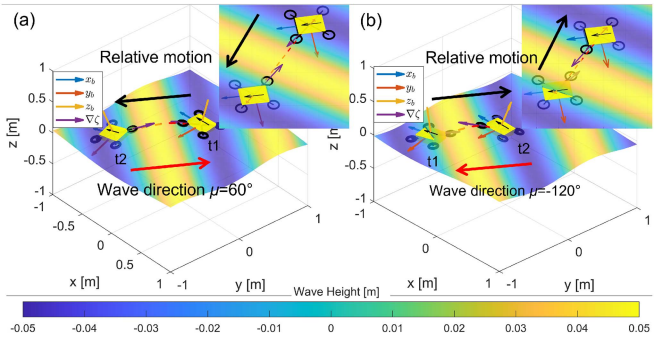

Fig. 8. Simulation of a single regular wave with different initial states. Actual wave direction in (a) is $\mu = 60°$, while $\mu = -120°$(reversed) in (b). Both initial headings are $\psi_0 = -170°$. The purple arrow shows the wave gradient perceived by the vehicle. Vertical views are shown in the subplots.

is generally greedy in all error ranges, which facilitates quick determination of the main wave direction. In the later period, the inertia of β is significantly improved after the heading error $\overline{e_{\alpha\psi}}$ exceeds 45°. The algorithm tends to be conservative, which benefits the convergence of heading. The convergence rate of the algorithm in different periods can be regulated by tuning the parameters or function types of β and γ.

3) Heading Server: The HS is realized by two stern-mounted horizontal marine thrusters of the vehicle, and the deviation of speed is calculated by the PID controller of the yaw channel, as shown in Algorithm 4. Meanwhile, the vehicle will keep advancing with the constant thrust from the marine thrusters, rather than just adjusting heading in situ. This is due to the fact that the crest of an irregular wave does not remain constant during its propagation, but rather shifts shapes as it spreads and dissipates. As a result, persistent propulsion can improve search efficiency and speed up the convergence.

4) Initial Conditon: The vehicle will encounter $\|\nabla\zeta\|_{\text{lmax}}$ twice in a wave cycle, once during the phase from trough to crest and once during the opposite phase. Therefore, one of the estimated wave directions α is upstream and the other is downstream. Hence, the vehicle will go upstream according to the acute angle constraint in Algorithm 3, if there is an obtuse angle in the bias between the original vehicle heading and the actual wave direction, exactly contrary to our expectation. As a result, the initial maneuver of the vehicle, that is, the judgment of the half sector in the downstream direction, is of global significance. Simulation is carried out through the single regular wave model in Section II in Fig. 8 to explore the solution for initialization.

Fig. 8 shows the vehicle attitude, relative motion, and the estimated wave gradient $\nabla\zeta$ when $||\nabla\zeta||$ reaches the first two local maximums in the first wave period. During the period $[t_1, t_2]$, the vehicle rises and then falls as the wave passes. The simulation results show that the maximum value of $||\nabla\zeta||$ reaches at time t_2 (descending from crest to trough) is always larger than that at time t_1, as shown in the length of the purple vector in Fig. 8. Meanwhile, the estimated direction at t_2 is the actual wave direction. The same rule applies when the algorithm is activated while the vehicle is descending. The reason is that the vehicle ascends with the wave in a manner similar to a passive lift. The vehicle's draft is larger [as shown at t_1 in Fig. 8(b)], and its attitude is less sensitive to waves. Whereas the vehicle's draft is smaller and the attitude response is more obvious when descending from the crest. In consequence, the α corresponding to the largest of the first N $||\nabla\zeta||_{\text{lmax}}$ is regarded as the initially estimated wave direction, as shown in Algorithm 5. $N \geq 2$ is set generally.

Algorithm 4: Heading Server (HS).

Input: Desired heading ψ_d, current heading ψ
Output: Increment of the pulsewidth modulator (PWM) of marine thrusters ΔPWM $_1$, Δ PWM$_2$
1: static initial $e_{\psi\text{last}}$
2: $e_\psi = \psi_d - \psi$
3: $e_\psi = e_\psi - 2\pi\text{sgn}(e_\psi)(|e_\psi| > \pi)$
4: $u_\psi = k_p e_\psi + k_i \sum_k e_\psi + k_d(e_\psi - e_{\psi_{\text{last}}})/\Delta t$
5: $\Delta\text{PWM}_1 = -u_\psi$, Δ PWM$_2 = u_\psi$

Algorithm 5: Initial Condition.

Input: $\|\widetilde{\nabla\zeta}\|$, α
Output: ψ_d
1: static loop number $n = 1$
2: $\|\nabla\zeta\|_{\text{sup}}[n] = \|\widetilde{\nabla\zeta}\|$
3: $\alpha_0[n] = \alpha$
4: **if** $n == N$ **then**
5: $\quad\psi_d = \alpha_0[\max\{\|\nabla\zeta\|_{\text{sup}}\}.n]$
6: **end if**
7: $n++$

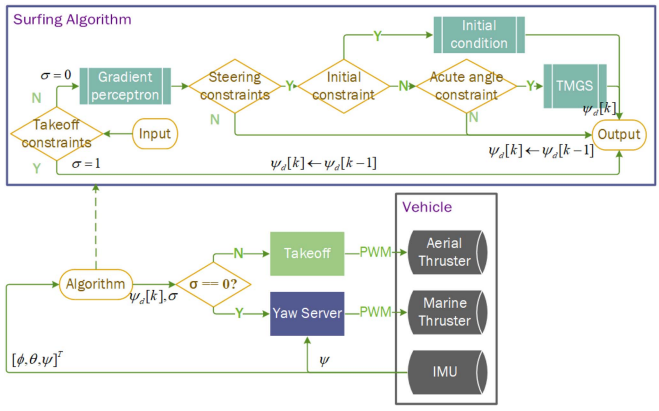

Fig. 9. Flow chart of the SA.

5) Outline: All the submodules and constraints of the algorithm have been introduced so far. The outline of the SA is listed in Algorithm 6 and the flowchart is shown in Fig. 9.

The whole test process is divided into four stages: drifting, surfing, taking off, and flying. The first three stages are completely autonomous. The SA including the yaw server (marked in dark blue in Fig. 9) is preuploaded on the underwater controller. The control and decision signals are generated by the microprogrammed control unit autonomously. When the logical

Algorithm 6: Outline of Surfing Algorithm (SA).

Input: $\boldsymbol{\Theta}[k] = \{\phi[k]\ \theta[k]\ \psi[k]\}^T \in \mathbb{R}^{3\times 1}, k \in \mathbb{N}^+$ from IMU

initial logical takeoff sign $\sigma = 0$, $\psi_d[1] = \psi[1]$
while $k \geq 1$ **do**
  $\boldsymbol{\Theta} \leftarrow \boldsymbol{\Theta} \cup \boldsymbol{\Theta}[k]$
  if $\sigma == 0$ **then**
    $\{\alpha[k], \|\widetilde{\nabla\zeta}\|[k]\}$ = **Gradient perceptron** ($\boldsymbol{\Theta}[k]$)
    $\psi_d[k] = \psi_d[k-1]$
    if Steering constraints (19) are satisfied **then**
      initial $n = 0, n++$
      if $n \leq N$ **then**
        $\psi_d[k]$ = **Initial condition**($\|\widetilde{\nabla\zeta}\|[k-1]$, $\alpha[k-1]$)
      else
        $\psi_d[k]$ =**TMGS**($\psi[k], \alpha[k-1]$)
      end if
    end if
    if Takeoff constraints (16) are satisfied **then**
      $\sigma \leftarrow\sim \sigma$
    else
      Heading server($\psi_d[k], \psi[k]$)
    end if
  else
    Takeoff()
  end if
  $k++$
end while

takeoff sign $\sigma = 1$, the takeoff is triggered. The flight part is executed on the open source Pixhawk flight controller. It follows the basic cascade PID control law and is independent of the SA. The takeoff command sent to the flight controller by the underwater control board is a stepped pulsewidth modulator (PWM) throttle. The amplitude is 10% more than the throttle required for a smooth takeoff from level ground. Once the vehicle is completely off the wave surface (successful takeoff), the vehicle is switched to manual mode to ensure safety. The signal input at this time is changed to the remote control. The SA does not require prior vehicle and wave information but relies on real-time attitude data obtained by IMU and open source flight controller, which is low-cost and easily deployed.

IV. Simulation

A. Regular Wave

The dynamic model in Section II and SA in Section III are simulated preliminarily under a single regular wave. The initialization is shown in Table II. Random disturbance moment, which follows a positive distribution with a mean of zero is added in (5) to simulate the effect of disordered waves on the attitude. The initial heading of the vehicle is $\psi_0 = -150^\circ$ and is at an obtuse angle to the actual wave direction that $\mu = 60^\circ$. The kinematic response is shown in Fig. 10. The blue curves

TABLE II
Initial Parameters of the Simulation in Regular Wave

Meaning	Symbol	Value	Unit
Wave parameters	$[h, \omega, \mu, \varepsilon]$	[0.06m, 7rad/s, 60°, 0]	\
Position	$[x_0, y_0, z_0]$	[−0.75, −0.2, 0]	m
Attitude	$[\phi_0, \theta_0, \psi_0]$	[0, 0, −150]	◦
Velocity	$[u_0, v_0, w_0]$	[0, 0 ,0]	m/s
Angular rate	$[p_0, q_0, r_0]$	[0, 0 ,0]	rad/s
Sampling time	Δt	50	ms

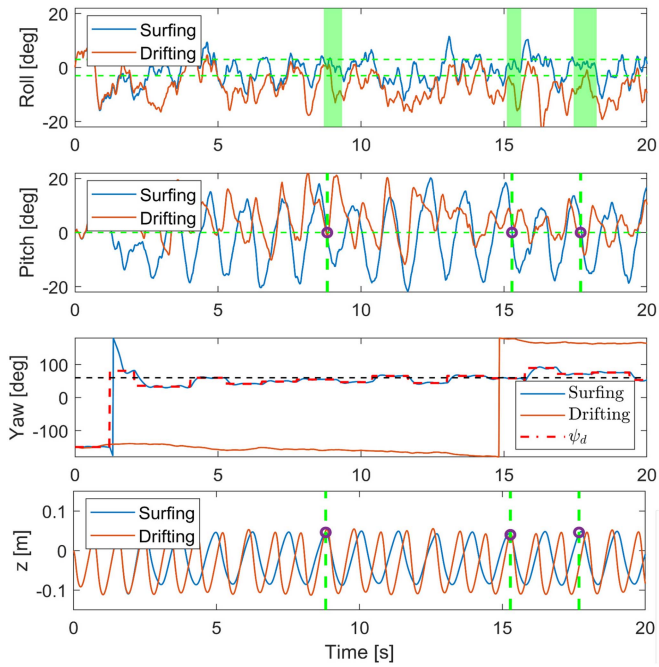

Fig. 10. Kinematic response under a single regular wave. Two green dashed lines within the roll subgraph are the steady limits of roll, and the green shadows are the zones where roll is relatively steady. In the subgraph of yaw, the black dashed line is the actual wave direction that $\mu = 60^\circ$. Purple circle is the time window that meets the takeoff constraints.

represent the case with SA, whereas the orange curves indicate the drifting case without SA.

The vehicle is at the crest when the takeoff constraints (16) are satisfied as the purple circles marked, which verifies the proposed sufficient conditions of takeoff. Although the amplitude of pitch is somewhat raised by the algorithm, the amplitude of roll is drastically weakened and fluctuates around 0°. The responses of roll and pitch become more regular than that without the algorithm. The number of the takeoff windows is increased from 0 to 3. Within the three windows, the heading estimation and tracking are convergent with an error of less than 10°. This verifies the robustness of the SA and illustrates that the frequency of the takeoff window can be effectively increased through crest searching and tracking, thus enhancing the success rate of takeoff.

Two representative moments of heading update warrant discussion, as shown in detail in Fig. 11. At t_1 and t_2, the steering constraints (19) are satisfied. $e_{\alpha\psi}$ is large at t_1, the inertia factor β of the TGMS algorithm starts to work. The updated direction ψ_{dk+1} (green arrow) is levered considerably from the

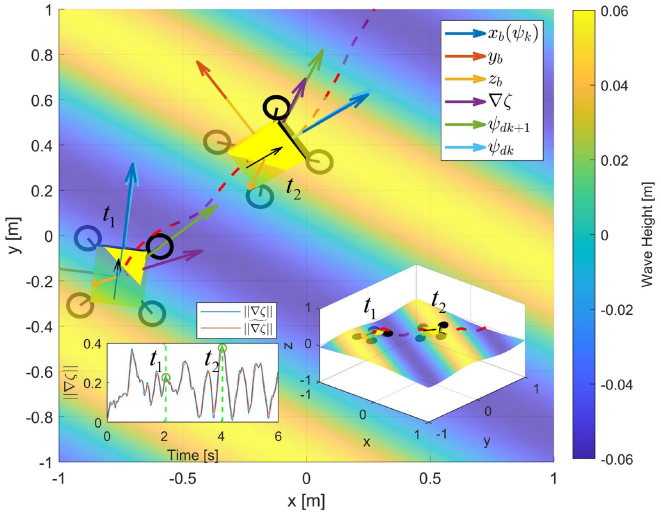

Fig. 11. Schematic diagram of the algorithm iteration. The absolute position, attitude and direction of each vector are depicted at the time of heading updates t_1 and t_2. The wave field is at time t_1. The 2D subgraph presents the time series of $||\nabla\boldsymbol{\zeta}||$ and the result of Kalman filter. The red dotted line is the absolute trajectory of the vehicle relative to the earth.

TABLE III
INITIAL PARAMETERS OF THE SIMULATION IN IRREGULAR WAVE

Meaning	Symbol	Value & Unit
Wave frequency band	$[\omega_{\min} : d\omega : \omega_{\max}\ ]$	[5:1:15] rad
Wave direction band	$[\mu_{\min} : d\mu : \mu_{\max}\ ]$	$[-90 : 30 : 90]^\circ$
Significant wave height	$h_{1/3}$	0.15 m
Average period	$\overline{T}$	1.5 s
Position	$[x_0, y_0, z_0]$	[−0.75, 0, 0] m
Attitude	$[\phi_0, \theta_0, \psi_0]$	$[0, 0, -150]^\circ$
Velocity	$[u_0, v_0, w_0]$	[0, 0 ,0] m/s
Angular rate	$[p_0, q_0, r_0]$	[0, 0 ,0] rad/s
Sampling time	Δt	50 ms

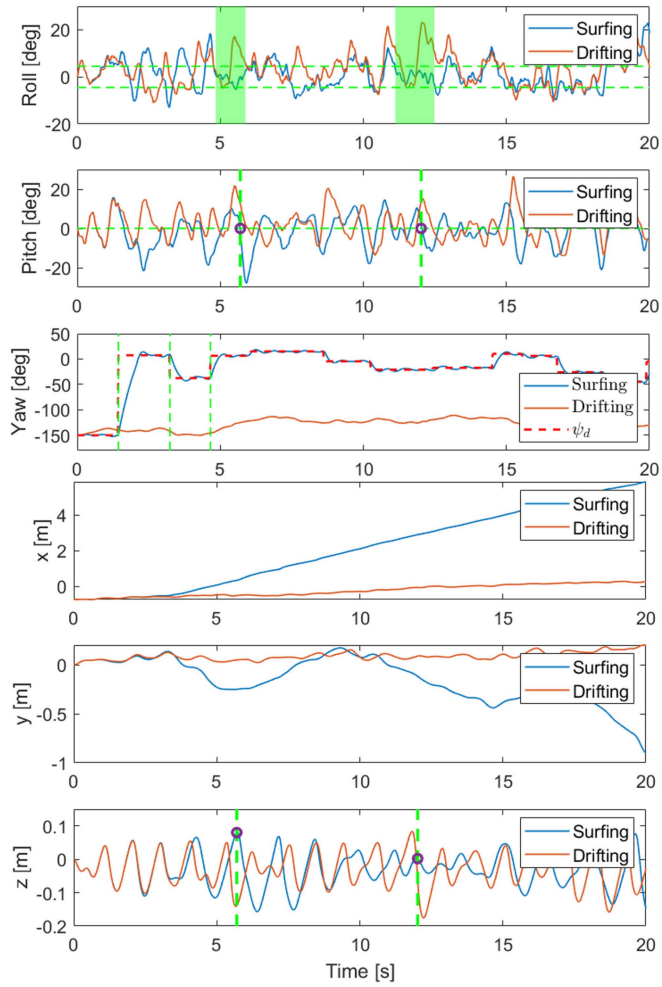

Fig. 12. In total, 6 DOF kinematic response in irregular waves. Remarks for the curves are the same as in Fig. 10.

original estimate $\nabla\boldsymbol{\zeta}$ (purple arrow) to the previous heading ψ_{dk} (blue arrow). Thus, TGMS enhances the accuracy of the direction estimation of the SA. In contrast, $e_{\alpha\psi}$ is small at t_2. The algorithm tends to be greedy and adopts the estimated direction almost directly. The vehicle keeps searching downstream by adjusting the heading along the red dotted track. In addition, the filtering effect shows that some pseudo spikes with less apparent features can be eliminated, and the wave direction judgment is not unaffected.

B. Irregular Wave

The SA is simulated in irregular waves to approximate the real wave state and the 6DOF kinematic response is shown in Fig. 12. The parameters in the irregular wave model (7) and the initialization are set in Table III. The primary wave propagation is 0°, extending into the surrounding semicircular region, which is also at an obtuse angle to the initial heading. The SA remains valid in irregular waves so that the heading maintains asymptotic stability with respect to the primary wave direction effectively. Since the wave direction is dispersed randomly along the main direction, the stable interval zone is larger than that of the regular wave case. The roll and pitch also show the same rule in irregular waves with the aid of the algorithm, and the vehicle experiences two takeoff windows within 20 s.

The first three heading updates at the time t_1, t_2, and t_3 are presented in detail in Fig. 13. The estimated heading of the first steering is obtuse to the initial heading, which is accomplished by the initial conditions. $\|\nabla\boldsymbol{\zeta}\|_{\text{lim}}$ is set 0.2, so that the first three local maximum points of $\|\nabla\boldsymbol{\zeta}\|$ are filtered out. The initial conditions work at t_0 and t_1. As $\|\nabla\boldsymbol{\zeta}\|_{t_0} > \|\nabla\boldsymbol{\zeta}\|_{t_1}$, although the vehicle turns at t_1, the first desired heading is generated at time t_0. It is marked as the purple arrow toward the crest at t_1. Then, the vehicle keeps heading ψ_{d1} until t_2. The estimated heading at t_2 also points to the crest. It is also affected by the previous heading (blue arrow) but does not adopt the direction of the purple arrow completely. The trajectory (red dotted line) tends to drift downward after this steering. At t_3, the updated heading is determined by the combined effect of a larger and farther crest ahead of the vehicle and a smaller and closer wave on the left, thus achieving a compromise between the two directions. The heading recovers to the main wave direction gradually. At other times, when $\|\nabla\boldsymbol{\zeta}\|$ reaches local maxima except t_0 to t_3, the acute angle constraints are not satisfied or

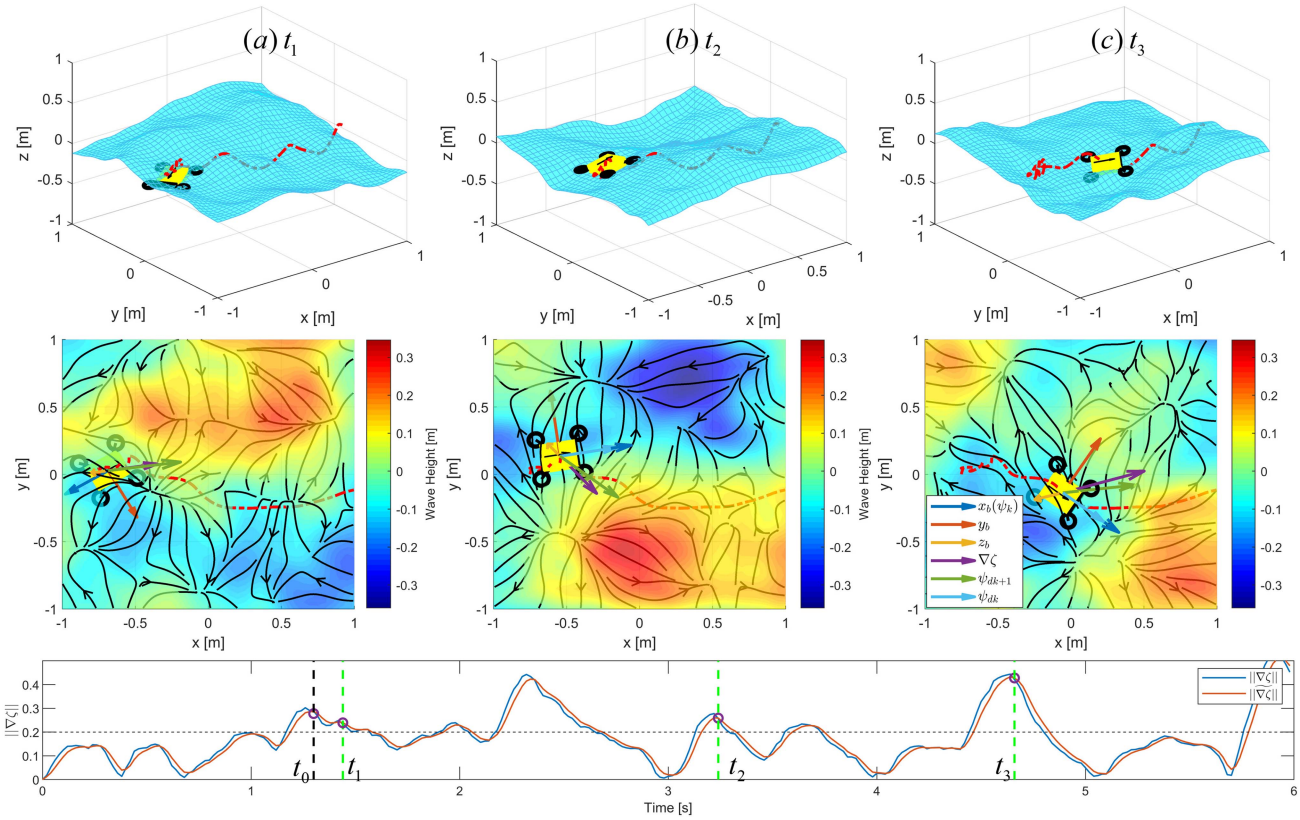

Fig. 13. State views of the vehicle and the wave field during the first three steerings.

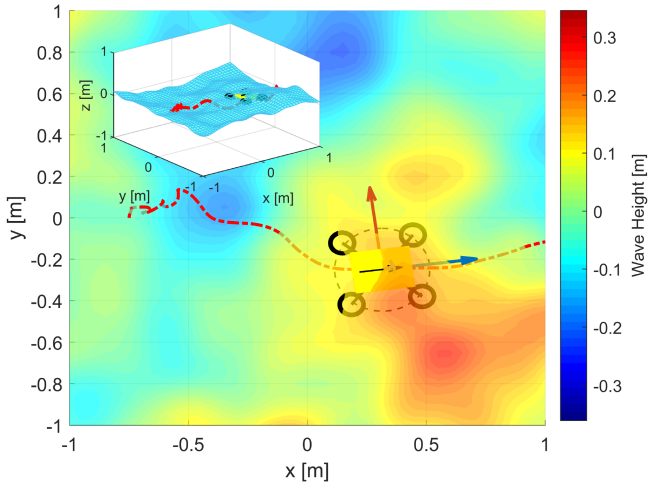

Fig. 14. Wave field and vehicle state at takeoff window.

the heading has not converged, so the desired heading is not updated.

At 5.7 s after the t_3 moment, the vehicle experiences the first takeoff window. The state and wave field at this time are shown in Fig. 14. The wave crest appears in the effective vicinity of the vehicle on its trajectory, and the vehicle heading aligns with the forward direction of the crest. The takeoff at this point will have a higher success rate.

V. Experiment

A. Regular Waves

The regular wave condition of 0.35 m height and 2 s cycle is adopted to test the effectiveness of the SA in the towing pool. The whole process is shown in Fig. 15.

The vehicle is drifting without control in the regular waves until the algorithm works at about 7.8 s. At time t_1 and t_2, the vehicle is located at points B and D of Fig. 5, respectively. The amplitude of acceleration is rising and falling, respectively. The wave direction $\mu = 0^\circ$ and the initial heading $\psi_0 = -130^\circ$. The limit interval of roll is set $\pm 2^\circ$ and the limit time is 1 s. $||\nabla\zeta||_{\text{lim}} = 0.1$. $||\boldsymbol{\nabla\zeta}||$ reaches the local maxima at t_1 and t_2 and $||\boldsymbol{\nabla\zeta}||_{t_1} > ||\boldsymbol{\nabla\zeta}||_{t_2}$. The estimated wave direction α matches with the actual direction μ at t_1 whereas it is inverse at t_2, which accords with the results of the initial conditions. At t_3, the estimated heading is adopted rather than that at t_2 and the surfing stage begins. The pitch amplitude is slightly increased but the roll is obviously attenuated. $||\boldsymbol{\nabla\zeta}||$ also reaches the local maxima at t_4 and t_6. However, at t_6 the acute angle constraints (20) takes effect, so the steering constraints (19) work at t_4 rather than t_6. Besides, the third heading update occurs at t_7. The heading estimation error at this time is less than 2°. The takeoff constraints (16) are not satisfied until t_8, the vehicle is at the crest with a stable attitude in Fig. 15 A. All four propellers generate valid cavitation after launching, and the acceleration changes from the weightless state at the crest to the overweight

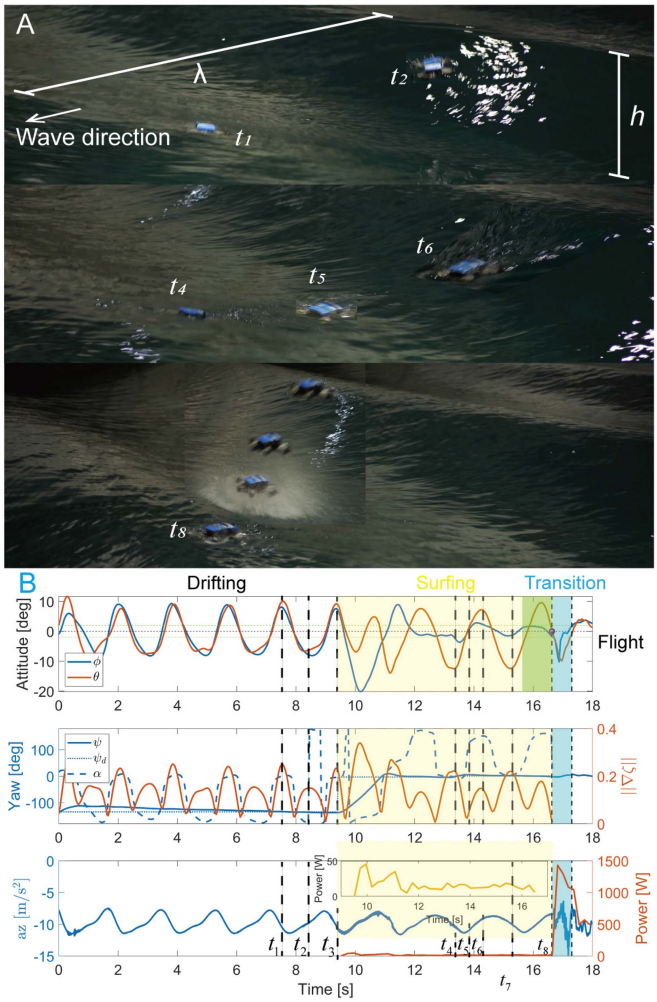

Fig. 15. A: Whole process of unpowered drifting, surfing, and taking off. B: State and energy consumption changes of the vehicle.

state dramatically. The whole process takes 7.1 s to surf and 0.57 s to take off. The energy consumption E is the integral of the product of voltage U and current I over time t. That is, $E = \int U(t)I(t)dt$. The peak power is about 1.4 kW. The energy cost during takeoff is about 655.2 J. The average power while surfing is 16.3 W, and the energy consumption is 116 J, which is much less (17.7%) than that of takeoff.

B. Irregular Wave

Field experiments in the irregular wave environment are carried out. The wave state is shown in Fig. 16. The swell and surge have preliminarily emerged and whitecap has locally formed. According to the camera imaging model in the field of image processing, the step with a length of about 30 cm is selected as the reference object. It can be roughly estimated that the wave height interval is concentrated in [0.2, 1] m, and the lowest wave height is three times the height of the vehicle.

The wave field and vehicle state during the surfing are pictured in Fig. 17(a), and the heading compass is shown in Fig. 17(d). The algorithm starts when the initial heading of the vehicle

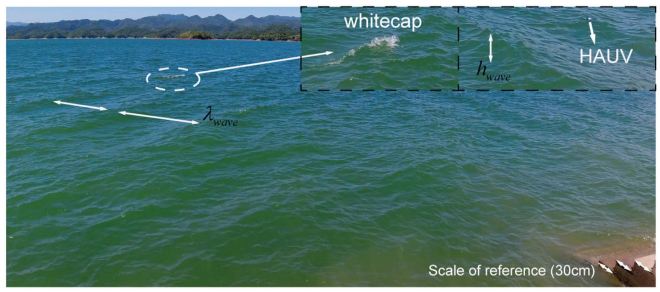

Fig. 16. Overview of the wave state and environment at the experiment site.

is $\psi_1 = 155°$, which is obtuse with the main wave direction $\mu_{\text{main}} = 15°$. The initial conditions in Algorithm 5 are valid, so that ψ and μ_{main} have roughly coincided until t_3. The vehicle is surrounded by the advancing waves. The crest gathers and diffuses continually, resulting in the vehicle adjusting heading and searching for crests in the range of about 30°, from t_3 to t_7. A local crest travels [circled in blue in Fig. 17(a), (g), and (h)] in the same direction as the vehicle heads at t_7. The takeoff constraints (16) are satisfied at t_8 subsequently, as marked in Fig. 17(c). The vertical acceleration a_z reaches a local maximum and $a_z > -g$ at t_8, which means the vehicle is weightless and the sum of accelerations is downward, proving that the vehicle is at the wave crest. Fig. 17(a)–(h) also demonstrates the light draft and healthy attitude of the vehicle. The immersed aerial thrusters are activated at t_8, breaking the wave surface and generating upward thrust, thus, a_z falls dramatically and the vehicle is overweight. The propeller works in the mixed water–air medium with volatile dynamic characteristics [shown in Fig. 17(b)], resulting in the violent oscillation of a_z. The water–air mixture dissipates and the acceleration stabilizes gradually as the vehicle elevates from the surface agilely. The transition lasts about 0.75 s, indicating that the algorithm can enhance cross-domain safety and rapidity. The heading still remains parallel with the wave, and the roll and pitch tend to be stable after takeoff.

C. Contrasting Cases

Random takeoff experiments without the SA are also carried out as shown in Fig. 18. The aerial actuators are activated before the first crest (Crest 1) reaches. Neither the heading is downstream nor the initial attitude is healthy at t_1. Soon the propellers are slammed by Crest 1, resulting in the unsteady thrust at t_2. Meantime, the control proportion of the roll, pitch, and yaw channels vibrates dramatically and increased about twice as much as t_1. This part of the thrust is allocated for attitude recovery, reducing the original thrust applied to takeoff. Therefore, although the vehicle is mostly exposed to the air at t_3, when Crest 1 has left and Crest 2 has not arrived, the takeoff fails due to insufficient thrust. The following situation is similar. The vehicle is hit by Crest 2 at t_4 and also lacks thrust to takeoff at t_5 and then falls to the surface. The difference is that under the efforts of coping with Crest 1 (t_1 to t_3), the attitude during t_4 to t_6 has been roughly restored. Thus, the control proportion returns to its prior level. However, the takeoff is unaccomplished

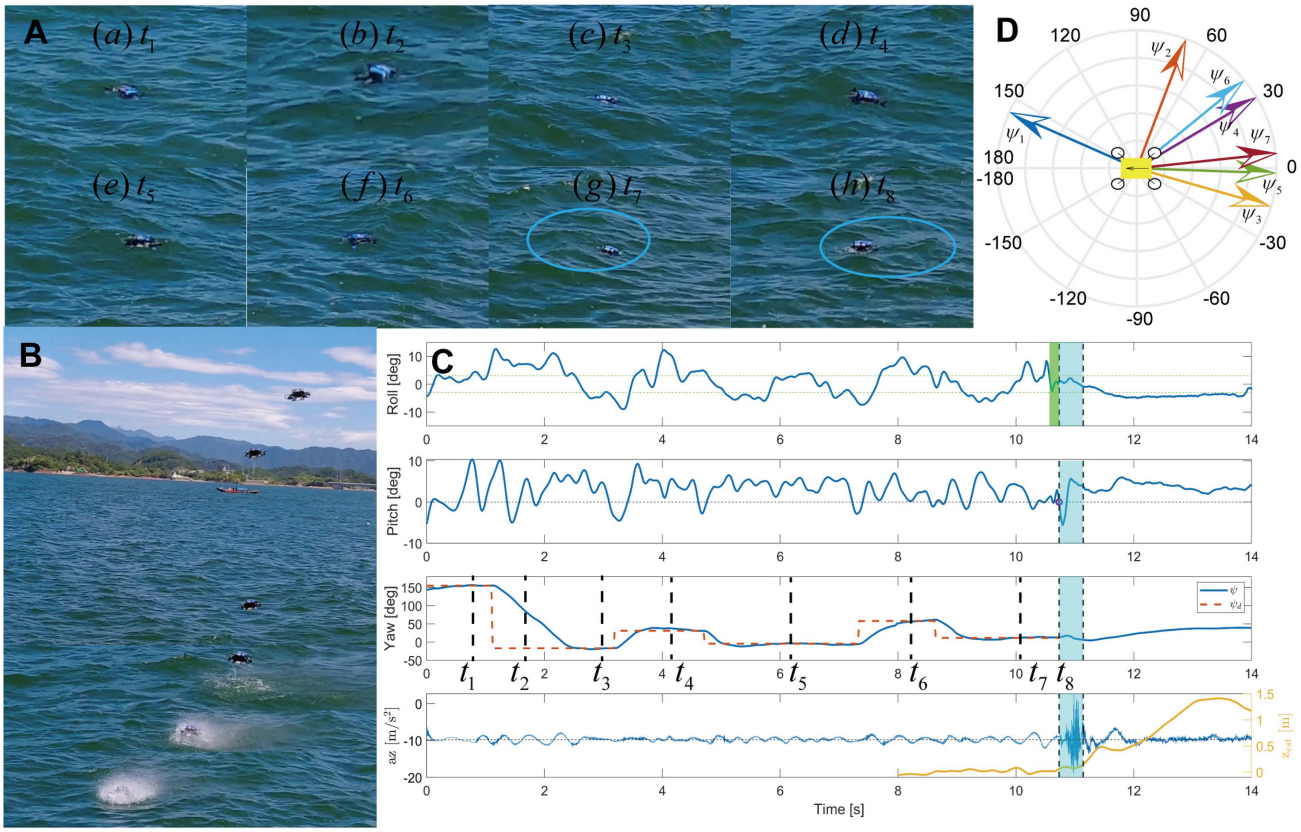

Fig. 17. Vehicle surfs (**A**) and takes off (**B**) in real irregular waves. Attitude, vertical acceleration a_z, and estimated altitude z_{est} are shown in **C**. t_1 to t_8 corresponds to (a)–(h) in **A**. Heading compass is shown in (**D**) with ψ_1 to ψ_7 corresponding to t_1 to t_7 in (**A**).

at t_6 because the thrust is still cut down by the unstable dynamic characteristics of the –air mixture. The waves have moved away until t_7. At this moment, the surface is relatively calm, and the properties of the mixture tend to be stable, so that the takeoff condition is ideal. Although the cross-domain ultimately succeeds, the entire transition costs 3.8 s, about 5 times as much as surfing (0.75 s).

The control proportion with SA in Fig. 17 is also shown in Fig. 18(c). It vibrates intensely at the moment when takeoff is triggered to mitigate the inevitable instability caused by the varying dynamics. The control proportion tends to be low and stable rapidly with SA. The average peak proportion of the three attitude channels in the case without SA is about 2.3 times larger than the case with SA and the duration is significantly longer, indicating that the algorithm effectively avoids the distraction of the controller and makes the thrust concentrate on the takeoff. Besides, the control proportion of the yaw channel with SA is noticeably lower than that of the other two channels, despite being considerable in the absence of SA. Moreover, the peak proportion of yaw channel without SA is about four times larger than that with SA. The risk that a wave hits a single propeller increases when the takeoff is triggered at a random heading. The motor torque changes abruptly after hitting, thus the controller has to distribute thrust to the yaw channel to prevent spinning. The SA guides the vehicle to take off downstream at wave crest, so that as much thrust as possible is focused on the elevation rather than the uncertainty. First, the takeoff constraints ensure a healthy attitude of vehicle and balanced immersion of propellers. Second, the vehicle is inaccessible to being hit by other waves at the crest, which avoids unnecessary wave disturbance. As a result, the takeoff process is more lithe and smooth, enhancing maneuverability and safety.

A series of regular wave experiments are carried out in the towing pool for energy consumption analysis. Four typical positions shown in Fig. 5 are selected. The wave height is set to 0.35 m with a period of 2.0 s. Two groups of experiments (I: downstream takeoff; II: random takeoff) are carried out at the four positions and experiments are performed three times for each case. The initial headings are random for each time of Group II. Fig. 19 displays the scenes when takeoff begins. The time and power cost data are shown in Table IV. The data in parentheses represent the time and energy of surfing.

The energy consumption is mainly used for breaking the wave surface, stabilizing attitude, and climbing during the cross-domain stage. The energy is mainly converted into kinetic and gravitational potential energy of the fluid and the vehicle. Fig. 15 B shows the relative amplitude of energy consumption changes during the whole process of surfing and taking off. The average surfing power and time of Case A.I is 16.6 W and 6.2 s, respectively, and the average energy consumption is 103 J, which is just approximately 20% of the energy consumption of the

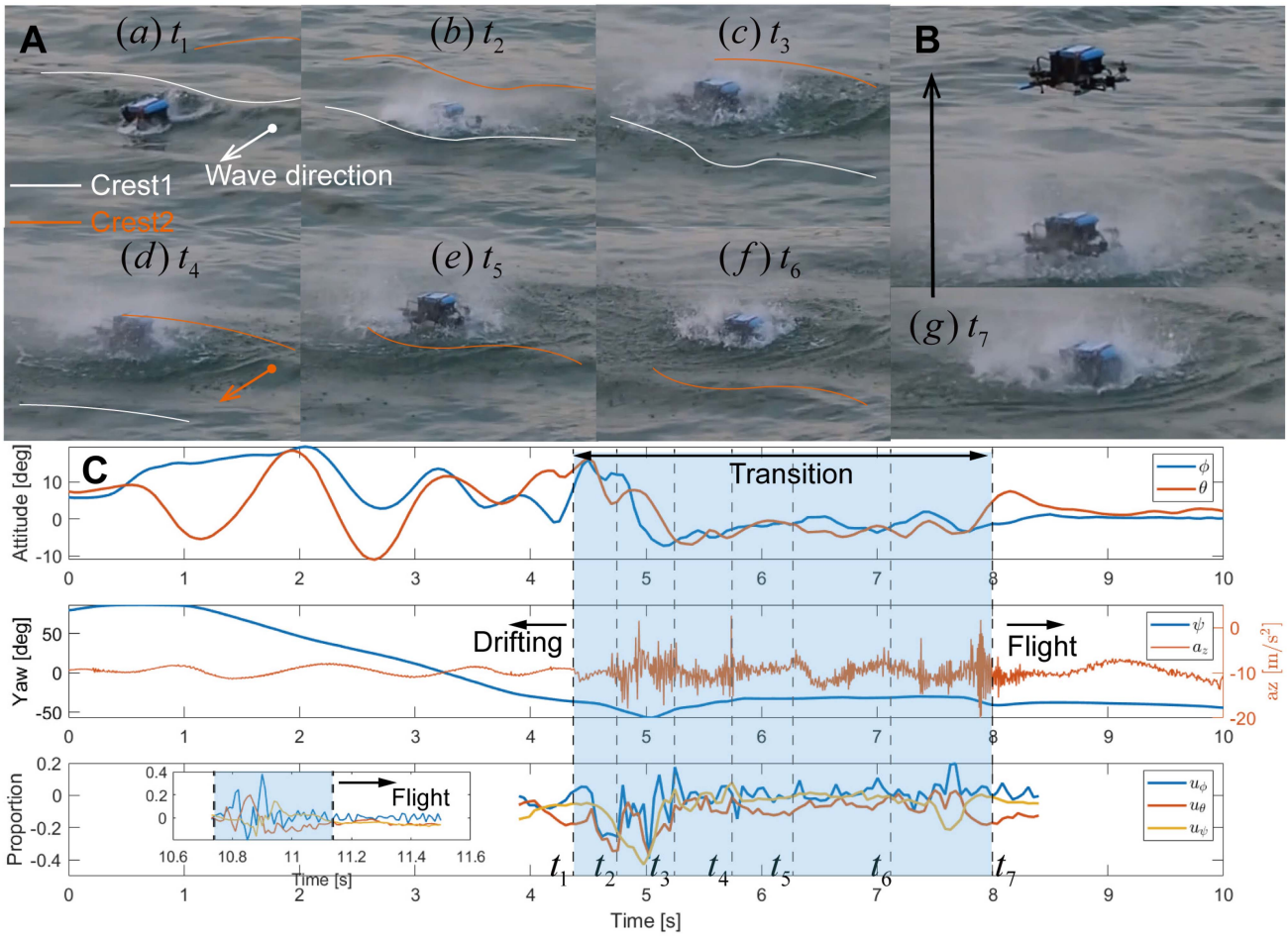

Fig. 18. Vehicle drifts (**A**) and takeoffs randomly (**B**) in irregular waves. Attitude, vertical acceleration a_z, and the control proportion of roll, pitch, and yaw channels calculated by flight controllers to their respective saturation values are shown in **C**. Subplot is the proportion of the case in Fig. 17. t_1 to t_7 corresponds to (a)–(g) in **A**. First arrived crest (Crest 1) and the following crest (Crest 2) are marked in the white and orange lines, respectively.

TABLE IV
COMPARISON OF TIME AND ENERGY COSTS FOR DIFFERENT TAKEOFF CASES

Position	Case	Maximum takeoff time /s	Average takeoff time /s	Maximum energy cost /J	Average energy cost /J
/	Ground	0.24	0.23	356.8	348.5
/	Calm water	0.51	0.48	532.1	517.4
A	I	0.64	0.58	695.3 (+114)	668.8 (+103)
	II	1.69	1.1	1140.2	915.8
B	I	1.11	1.01	937.6	883.6
	II	1.37	1.20	1027.6	955.3
C	I	1.07	0.98	898.3	864.3
	II	4.25	2.07	2186.2	1304.2
D	I	3.59	1.78	1874.2	1185.7
	II	2.18	1.82	1388.5	1206.2

calm water takeoff situation. The total energy consumption is still the lowest in all eight cases. Although the surfing time is increased, the energy cost is significantly reduced. When taking off downstream (Group I), the vehicle's roll is leveled off at all four positions, weakening the burden on the controller. The average takeoff time and energy consumption are reduced by 29.7% and 17.8%, respectively, compared with Group II. Furthermore, the vehicle attitude at A and C points is more stable than that at B and D points, thus the time and energy costs are lower.

The likelihood that the propellers will be unevenly exposed to air or immersed in water increases when taking off randomly (Group II), and the initial attitude is unhealthy. The subsequent waves introduce persistent disturbance during the time that addresses the aforementioned uncertainties, so the time and power costs are larger at each position compared with Group I. In the C-D-A phase, the vertical velocity of the wave particle is upward in Fig. 5. The wave surface is rising and advancing, and the vehicle is more likely to be hit by subsequent waves, thus the time and energy costs are further enlarged. The wave surface after takeoff at the crest is in a downward trend, which facilitates the vehicle's water-exit process.

SA is not dominant in terms of considering the total time cost, since surfing occupies the majority of the time (92.6% in Fig. 15). But in the scenario of more hazardous wave conditions or inappropriate takeoff opportunities, the time cost of random takeoff can be prolonged indefinitely, and even the safety is threatened by the risk of capsizing and takeoff failure. The

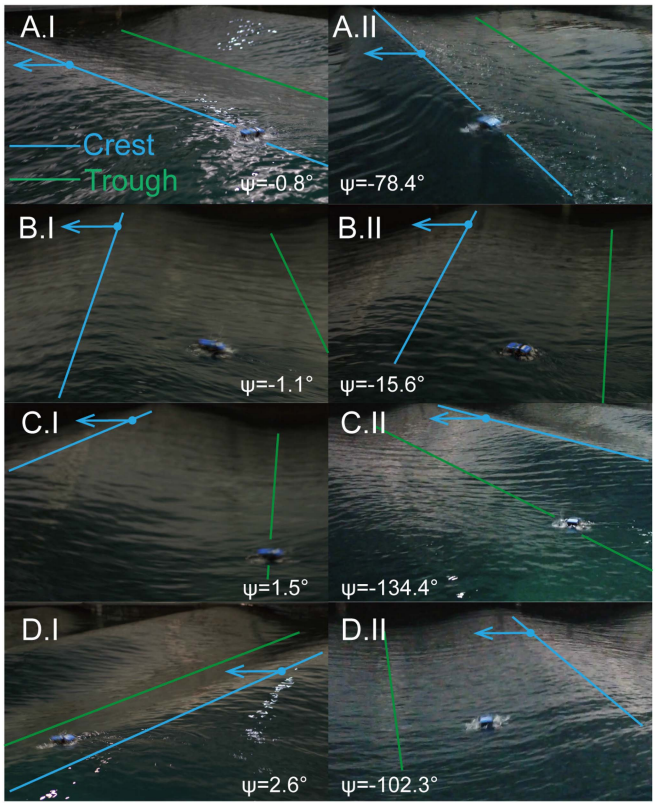

Fig. 19. Positions and headings when the takeoff is activated.

supplementary video shows some failure cases. From a safety point of view, the time cost of surfing is low compared with the cost of capsize. From the perspective of energy consumption, the underwater thruster is much more energy-saving during surfing compared with taking off directly for an extended duration. As a result, the surfing time is low cost and necessary. The takeoff time defined in this article is the time from the trigger of the signal to the complete departure of the vehicle from the wave surface, excluding the surfing time.

Taken together, surfing reduces the dimension of control and the uneven propeller immersion, and taking off at the crest avoids the unhealthy initial attitude and subsequent wave slamming. Therefore, the time and energy consumption with the SA is more favorable. Compared with the average of the other seven cases, the time and energy costs of Case A.I are reduced by 59.2% and 26.1%, respectively. Compared with the specific case, the costs are reduced by 84.9% and 63.5%, respectively. The increase in time and energy consumption with the SA is only 10.6% and 46.5% of the average increment of the other seven cases, respectively, as compared with the still-water takeoff case.

Greater thrust redundancy allows larger vehicles to handle more severe wave disturbances. But in harsh sea conditions, the height of the swell can reach more than 2 m, accompanied by dissipation and fragmentation. The frequency is more random. In this scenario, the scale of the large vehicle is still small relative to the wave, and the attitude response is more drastic, so the cross-domain takeoff faces safety risks. It is still meaningful to search for a suitable cross-domain window. SA has the adaptability of large vehicles in theory. The relative scale of waves and vehicles is an interesting research direction. Extending it to a larger prototype and carrying out experiments in sea state above level three is one of our next research goals.

VI. Conclusion

In this article, a cross-domain strategy for HAUVs in wave-dominated environments is proposed that utilizes quiescent periods search to travel on advantageous wave crests. The vehicle-wave coupling response is modeled and developed. The characteristics and mechanisms of the cross-domain dynamic window are summarized for the first time. On this basis, the outline of the SA is proposed and simulated. The SA is implemented on the multirotor HAUV prototype Nezha-mini. The vehicle is able to sense the desired orientation of the dynamic window, then steers through the HS, and makes the takeoff decision downstream at the wave crest.

The field experiment matches well with the simulation, which verifies the effectiveness of the SA. Compared with the case of taking off at random timings and headings, the algorithm significantly reduces the distraction of uncertainty on thrust distribution during takeoff, such as wave interference and unhealthy attitude. The recovery control proportion of the three attitude channels is approximately halved, and the settling time is drastically shortened. As the thrust concentrates on the takeoff, the average transition time is less than 1 s, about 40% of the random takeoff, and the total energy consumption is reduced by 26.1% on average. Besides, the risk of takeoff failure is also reduced. The SA is independent of the physical model of both the vehicle and waves and is easy to deploy. This allows safe and agile cross-domain locomotion without requiring a high-precision IMU and a robust flight controller. The surfing strategy provides an enlightening methodology for HAUV crossing over the wave surface.

Acknowledgment

The authors would like to thank Hongfei Xie for his support on the pool experiments. The authors would also like to thank Zhihao Fan and the fellows from the Smart Ocean Laboratory of Dalian University of Technology for their support on the field experiments. They also thank Qingbo Liu for his support on the language proofreading.

References

[1] X. Yang, T. Wang, J. Liang, G. Yao, and M. Liu, "Survey on the novel hybrid aquatic–aerial amphibious aircraft: Aquatic unmanned aerial vehicle (aquaUAV)," *Prog. Aerosp. Sci.*, vol. 74, no. 4, pp. 131–151, 2015.

[2] X. Ma, G. Wang, and K. Liu, "Design and optimization of a multimode amphibious robot with propeller-leg," *IEEE Trans. Robot.*, vol. 38, no. 6, pp. 3807–3820, Dec. 2022.

[3] K. L. Walker, A. A. Stokes, A. Kiprakis, and F. G.-Serchi, "Feed-forward disturbance compensation for station keeping in wave-dominated environments," in *Proc. OCEANS*, Limerick, Ireland, 2023, pp. 1–7.

[4] T. Wei et al., "Experimental study on trans-media hydrodynamics of a cylindrical hybrid unmanned aerial underwater vehicle," *Ocean Eng.*, vol. 252, 2022, Art. no. 111190.

[5] Y. H. Tan and B. M. Chen, "Motor-propeller matching of aerial propulsion systems for direct aerial-aquatic operation," in *Proc. IEEE/RSJ Int. Conf. Intell. Robots Syst.*, 2019, pp. 1963–1970.

[6] I. Y. Semenov, "Development of hybrid air-water rotor transition thrust prediction and control," Ph.D. dissertation, Univ. of Maryland, College Park, MD, USA, 2020.

[7] Z. Zeng, C. Lyu, Y. Bi, Y. Jin, D. Lu, and L. Lian, "Review of hybrid aerial underwater vehicle: Cross-domain mobility and transitions control," *Ocean Eng.*, vol. 248, 2022, Art. no. 110840.

[8] Y. Chen et al., "A biologically inspired, flapping-wing, hybrid aerial-aquatic microrobot," *Sci. Robot.*, vol. 2, no. 11, 2017, Art. no. eaao5619.

[9] R. Zufferey et al., "Consecutive aquatic jump-gliding with water-reactive fuel," *Sci. Robot.*, vol. 4, no. 34, 2019, Art. no. eaax 7330.

[10] R. Siddall, A. O. Ancel, and M. Kovač, "Wind and water tunnel testing of a morphing aquatic micro air vehicle," *Interface focus*, vol. 7, no. 1, 2017, Art. no. 20160085.

[11] W. Weisler, W. Stewart, M. B. Anderson, K. J. Peters, A. Gopalarathnam, and M. Bryant, "Testing and characterization of a fixed wing cross-domain unmanned vehicle operating in aerial and underwater environments," *IEEE J. Ocean. Eng.*, vol. 43, no. 4, pp. 969–982, Apr. 2017.

[12] F. M. Rockenbauer et al., "Dipper: A dynamically transitioning aerial-aquatic unmanned vehicle," in *Proc. Robot.: Sci. Syst.*, 2021, 1–9.

[13] J. Moore, A. Fein, and W. Setzler, "Design and analysis of a fixed-wing unmanned aerial-aquatic vehicle," in *Proc. IEEE Int. Conf. Robot. Automat.*, 2018, pp. 1236–1243.

[14] R. Zufferey et al., "SailMAV: Design and implementation of a novel multimodal flying sailing robot," *IEEE Robot. Automat. Lett.*, vol. 4, no. 3, pp. 2894–2901, Mar. 2019.

[15] D. Lu et al., "Design, fabrication, and characterization of a multimodal hybrid aerial underwater vehicle," *Ocean Eng.*, vol. 219, 2021, Art. no. 108324.

[16] C. Lyu et al., "Toward a gliding hybrid aerial underwater vehicle: Design, fabrication, and experiments," *J. Field Robot.*, vol. 39, no. 5, pp. 1–14, 2022.

[17] L. Li et al., "Aerial-aquatic robots capable of crossing the air-water boundary and hitchhiking on surfaces," *Sci. Robot.*, vol. 7, no. 66, 2022, Art. no. eabm 6695.

[18] M. M. Maia, D. A. Mercado, and F. J. Diez, "Design and implementation of multirotor aerial-underwater vehicles with experimental results," in *Proc. IEEE/RSJ Int. Conf. Intell. Robots Syst.*, 2017, pp. 961–966.

[19] P. L. J. Drews, A. A. Neto, and M. F. M. Campos, "Hybrid unmanned aerial underwater vehicle: Modeling and simulation," in *Proc. IEEE/RSJ Int. Conf. Intell. Robots Syst.*, 2014, pp. 4637–4642.

[20] H. Alzu'bi, I. Mansour, and O. Rawashdeh, "Loon Copter: Implementation of a hybrid unmanned aquatic–aerial quadcopter with active buoyancy control," *J. Field Robot.*, vol. 35, no. 5, pp. 764–778, 2018.

[21] A. A. Neto, L. A. Mozelli, P. L. J. Drews, and M. F. M. Campos, "Attitude control for an hybrid unmanned aerial underwater vehicle: A robust switched strategy with global stability," in *Proc. IEEE Int. Conf. Robot. Automat.*, 2015, pp. 395–400.

[22] Y. Chen, Y. Liu, Y. Meng, S. Yu, and Y. Zhuang, "System modeling and simulation of an unmanned aerial underwater vehicle," *J. Mar. Sci. Eng.*, vol. 7, no. 12, p. 444, 2019.

[23] Z. Ma, J. Feng, and J. Yang, "Research on vertical air–water trans-media control of hybrid unmanned aerial underwater vehicles based on adaptive sliding mode dynamical surface control," *Int. J. Adv. Robotic Syst.*, vol. 15, no. 2, 2018, Art. no. 1729881418770531.

[24] Q. Chen, D. Zhu, and Z. Liu, "Attitude control of aerial and underwater vehicles using single-input fuzzy PID controller," *Appl. Ocean Res.*, vol. 107, 2021, Art. no. 102460.

[25] D. Lu, C. Xiong, Z. Zeng, and L. Lian, "Adaptive dynamic surface control for a hybrid aerial underwater vehicle with parametric dynamics and uncertainties," *IEEE J. Ocean. Eng.*, vol. 45, no. 3, pp. 740–758, Mar. 2019.

[26] D. Lu, Y. Guo, C. Xiong, Z. Zeng, and L. Lian, "Takeoff and landing control of a hybrid aerial underwater vehicle on disturbed water's surface," *IEEE J. Ocean. Eng.*, vol. 47, no. 2, pp. 295–311, Feb. 2021.

[27] A. Battiston, I. Sharf, and M. Nahon, "Attitude estimation for collision recovery of a quadcopter unmanned aerial vehicle," *Int. J. Robot. Res.*, vol. 38, no. 10–11, pp. 1286–1306, 2019.

[28] J. Riola, J. J. Diaz, and J. G.-Sierra, "The prediction of calm opportunities for landing on a ship: Aspects of the problem," in *Proc. IEEE OCEANS*, 2011, pp. 1–8.

[29] S. Abujoub, J. Mcphee, C. Westin, and R. A. Irani, "Unmanned aerial vehicle landing on maritime vessels using signal prediction of the ship motion," in *Proc. OCEANS IEEE MTS/IEEE Charleston*, 2018, pp. 1–9.

[30] Y. Gao, H. Yu, and J. Wu, "Launch scheme and control law design of small tube launched UAV," in *Proc. IEEE China Autom. Congr.*, 2021, pp. 8154–8158.

[31] E. Gokbel and S. Ersoy, "Launchable rotary wing UAV designs and launch mechanism designs for rotary wing UAV," *J. Mechatronics Artif. Intell. Eng.*, vol. 2, no. 2, pp. 102–113, 2021.

[32] Y. Bi, Y. Jin, C. Lyu, Z. Zeng, and L. Lian, "Nezha-mini: Design and locomotion of a miniature low-cost hybrid aerial underwater vehicle," *IEEE Robot. Automat. Lett.*, vol. 7, no. 3, pp. 6669–6676, Mar. 2022.

[33] Y. Bi, D. Lu, Z. Zeng, and L. Lian, "Dynamics and control of hybrid aerial underwater vehicle subject to disturbances," *Ocean Eng.*, vol. 250, 2022, Art. no. 110933.

Yuanbo Bi received the B.Eng. degree in naval architecture and ocean engineering from Harbin Engineering University, Harbin, China, in 2020. He is currently working toward the Ph.D. degree in marine science with Shanghai Jiao Tong University, Shanghai, China.

His research interests include hybrid aerial underwater vehicles and control.

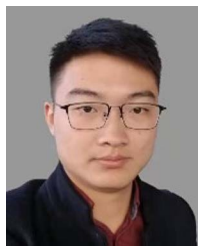

Yufei Jin (Graduate Student Member, IEEE) received the M.Sc. degree in advanced aeronautical engineering from Imperial College London, London, U.K., in 2019. He is currently working toward the Ph.D. degree with the School of Oceanography, Shanghai Jiao Tong University, Shanghai, China.

He research interest focuses on system design of hybrid aerial underwater vehicles now.

Hexiong Zhou received the bachelor's degree in electrical engineering and automation from Northwestern Polytechnical University, Xi'an, China, in 2015, the master's degree in control science and engineering from Harbin Engineering University, Harbin, China, in 2018, and the Ph.D. degree in naval architecture and ocean engineering from Shanghai Jiao Tong University, Shanghai, China, in 2022, respectively.

His research interests include path planning, optimal guidance, navigation, and tracking control of underwater vehicles.

Yulin Bai received the bachelor's degree in marine science from Shandong University, Weihai, China, in 2020, and the master's degree in marine science from the School of Oceanography, Marine Technology, Shanghai Jiao Tong University, Shanghai, China, in 2023.

His research interests include floats, hybrid aerial underwater vehicles, and embedded design.

Chenxin Lyu (Graduate Student Member, IEEE) received the B.Eng. degree in ocean technology from the Dalian University of Technology, Dalian, China, in 2019, and the M.Sc. degree in marine science, in 2022 from the School of Oceanography, Shanghai Jiao Tong University, Shanghai, China, where he is currently working toward the Ph.D. degree in marine science.

His research interests include underwater vehicles, hybrid aerial underwater vehicles, and adaptive control.

Zheng Zeng (Senior Member, IEEE) received the B.Eng. degree in electrical and electronic engineering from Hunan University, Changsha, China, in 2010, and the Ph.D. degree in ocean engineering from Flinders University, Adelaide, SA, Australia, in 2015.

He is currently an Associate Research Professor with Shanghai Jiao Tong University, Shanghai, China. His main research interests include autonomous marine vehicles, including optimal guidance, navigation, and control systems. He has led the research and development of Nezha I∼IV, Nezha-mini, Nezha-F and other series of hybrid aerial underwater vehicles (HAUVs), and has completed the HAUVs field tests in real ocean environment, with the maximum dive depth of 100 metres in the sea test. He has won a number of academic awards, such as the Top 10 Marine Science and Technology Advances of China in 2022, and the Shanghai Ocean Science and Technology Prize.

Lian Lian (Senior Member, IEEE) received the B.S. and M.S. degrees in naval architecture and ocean engineering and the Ph.D. degree in technology management from Shanghai Jiao Tong University, Shanghai, China, in 1982, 1985, and 2012, respectively.

She has been a Full Professor with Shanghai Jiao Tong University since 1998, and served as a Member with Expert Group of National Hi-Tech Program (863 Program) from 1999 to 2011, and a Member of Expert Group of the National Science Foundation of China, from 2008 to 2011. She is currently the Vice Dean with the Institute of Oceanography, Shanghai Jiao Tong University, and a Member of the IEEE/OES Administrative Committee, as well as the IEEE/OES Shanghai Chapter Chair. Her research interests mainly focus on underwater vehicles and marine observation.

Dr. Lian has been in charge of eight projects as PI/Chief Designer with total funding over 90 million RMB, which include national and municipal research projects funded by the National HiTech 863 Program, the National Key Project, the National Natural Science Foundation of China, the National R&D Program of Marine Technology, as well as the R&D Program of Science and Technology Committee of Shanghai Municipal Government.

IEEE Transactions on Robotics (T-RO) paper, presented at ICRA 2024, Yokohama, Japan. Cite as T-RO paper.